Multi-fluid approach for the numerical prediction of wall erosion in an elbow

Wenchao Yu, Pascal Fede, Éric Climent, Sean Sanders

Multi-fluid approach for the numerical prediction of wall erosion in an elbow

Wenchao Yu [a], Pascal Fede [a,*], Eric Climent [a], Sean Sanders [b]

[a] Institut de Mécanique des Fluides de Toulouse (IMFT), Université de Toulouse, CNRS, FR-31400 Toulouse, France
[b] Department of Chemical and Materials Engineering, University of Alberta, Edmonton, Alberta T6G 1H9, Canada

Multiphase pipeline flows are widely used in the oil and gas industry to transport solid liquid or gas solid mixtures. Erosion caused by the impact of solid particles is a major challenge for equipment maintenance and safety, especially in complex geometries such as elbows. In this work, a CFD study on wall erosion in a 90° standard elbow has been performed using a multi fluid approach, also called Euler/Euler, for poly dispersed fluid particle flows. A model is used for the erosion prediction taking into account particle turbulent kinetic energy obtained from the Euler Euler approach. A good agreement with experiments is observed. The effects of wall roughness and solid mass flow rate on the erosion rate are also investigated. For a certain amount of sand passing through the pipe elbow, there exists a solid mass flow rate for which the particle impact damage is most dramatic.

Keywords:
Euler-Euler approach
Erosion
Elbow
Numerical simulations

1. Introduction

Pipeline networks are widely used in the oil and gas industry to transport solid liquid or gas solid mixtures. Erosion caused by the dis persed solids is a major challenge for equipment maintenance and safety, especially in complex geometries such as valves and elbows. In such cases, better understanding of the erosion mechanism and accu rate prediction of the erosion rate in the different flow conditions are crucial.

Since the early investigations of particle impact erosion conducted by Finnie [1], understanding of single particle damage has been well de veloped. It can be briefly summarized that a micro cutting process dom inates at small impact angles and a deformation crack process dominates at large impact angles for ductile materials [2 4]. Based on these erosion mechanisms, many erosion models have been proposed and the influence of the relevant flow parameters and mixtures proper ties on erosion rate were investigated. Very detailed reviews about these advancements can be found, see, for example, Parsi et al. [5].

Particle impact erosion in elbows has been studied extensively dur ing the past few years. In numerical studies using Euler Lagrangian ap proaches, it has been reported that the erosion spatial distribution exhibits a “rabbit head” shape on the outer surface of the bend [6 13], which is formed by one main erosion region (corresponding to the rab bit face) centered at the extrados with two secondary erosion regions (corresponding to the rabbit ears) downstream of the main region. However, an elliptical erosion region, without secondary peaks, was ob served by Solnordal et al. [10] in their experiments.

The discrepancy between the CFD results and the experimental ob servations could be influenced by several parameters. By changing the particle wall bouncing model from Forder's model (coefficient of resti tution depends on impact angle [14]) to stochastic particle wall bounc ing model (coefficient of restitution calculated by an angle dependent distribution with angle dependent standard deviation [15]), Chen et al. [6] found that erosion in the main region is reduced and the second ary regions tend to disappear. Chen et al. [7] then kept the stochastic particle wall bouncing model but changed the carrier flow from air to water, and the secondary erosion regions disappeared completely. Pereira et al. [8] utilized three different particle wall bouncing models and three different wall roughness coefficients, which produced results that were different from the previous study. With the change from Forder's model to Grant and Tabakoff's stochastic model, erosion rate in the main region increased by 25%. Additionally, the secondary erosion regions did not change from smooth to rough walls. Numerical simula tions were also performed by Solnordal et al. [10]. It was found that the smooth wall assumption leads to inaccurate prediction of maximum erosion depth together with a “rabbit head” shaped erosion distribu tion, and by adopting a suitable rough wall collision model the erosion depth and distribution are much more accurately predicted. According to their results, maximum erosion depth decreases with increasing roughness. This is in contrast with the results of Pereira et al. [8] who found a negligible effect of the wall roughness, though the same rough ness model of Sommerfeld and Huber [16] was used for both studies. Duarte et al. [17] studied the coupling method and particle wall interac tion using the configuration of Solnordal et al. [10]. No secondary

* Corresponding author.
E-mail address: pascal.fede@imft.fr (P. Fede).

erosion regions were observed even with one way coupling (no inter particle collisions) when a suitable wall roughness model was activated, meaning that particle wall interaction has a major contribution to the particle dispersion in the near wall region. Moreover, the magnitude of maximum erosion is reduced with an increased roughness. The au thors explained that the particle wall interactions extract more mo mentum from particles when the wall is rough, which causes particles to hit the elbow surface with less energy, thereby reducing the erosion.

Mass loading has also an effect on the erosion spatial distribution. Bourgoyne [18] observed experimentally that the erosion rate was al most unchanged when increasing the solid mass flow rate (correspond ing to a maximum solid volume concentration 0.12%). Chen [19] varied the solid mass flow rate from 2.08×10^{-4} (corresponding to a solid vol ume concentration 0.05%) to 0.011 *kg/s* (corresponding to a solid vol ume concentration 2.44%), and the erosion rate decreased in their experiments. It was also observed in the experiments of Deng et al. [20] and Macchini et al. [21] that the erosion rate decreases when the solid volume concentration increases. Numerically, Duarte et al. [9,17] evaluated one , two and four way coupling modelling for different mass loadings. The secondary erosion regions tend to disappear when increasing the mass loading with four way coupling, due to the effects of inter particle collisions. They also found that the maximum erosion rate is gradually reduced as the mass loading increases. The authors at tributed this observation to a hindering effect due to the build up of a layer of particles adjacent to the wall, protecting elbow from direct par ticle collisions. Xu et al. [12] investigated the effect of solid mass flow rate and coupling method on erosion in an elbow. When increasing the solid mass flow rate, the secondary erosion regions disappear due to the inter particle collisions which is in agreement with the simula tions of Duarte et al. [9]. The maximum erosion rate remained constant when solid mass flow rate was varied from 0.208×10^{-3} to 0.208×10^{-1} *kg/s*, but then increased at 0.208 *kg/s*, which contradicts the re sults of Duarte et al. [9]. The authors explained that the particles form a dynamic layer near the wall and the sliding of this dynamic particle layer may be the major reason for the increase of erosion rate at the highest solid mass flow rate.

In general, the effects of particle wall and particle particle interac tions on the erosion are not very clearly understood since conflicting results have been observed. There are still some open issues, for ex ample the competition of shielding effect and sliding effect of the particle layer that forms close to the elbow wall at high solid mass flow rates.

All CFD studies cited previously are based on Eulerian Lagrangian approach, which is easy to couple with empirical erosion models [5] based on the instantaneous velocity of each impacting particle. How ever, the computational cost makes this approach infeasible for high particle concentrations or multiphase flows in realistic engineering ap plications. Conversely, the Euler Euler approach is ideal for these kinds of problems. Solid particles are modeled as a continuum in an Eulerian framework so only the average properties of particles in each local cell are provided. To the best of the authors' knowledge, there are only a few studies using Euler Euler models for erosion prediction [22,23]). Messa et al. [22] proposed a mixed Euler Euler/Euler Lagrange ap proach to perform particle tracking within certain subdomains adjacent to the wall. The application of this new approach can predict erosion depth and spatial distribution in jet impingement and choke valve con figurations. Messa and Malavasi [23] developed a numerical methodol ogy to update the eroded wall surface in real time which would change the impact angle at each time step and consequently affect the erosion. However, the particle turbulent kinetic energy is not calculated by their

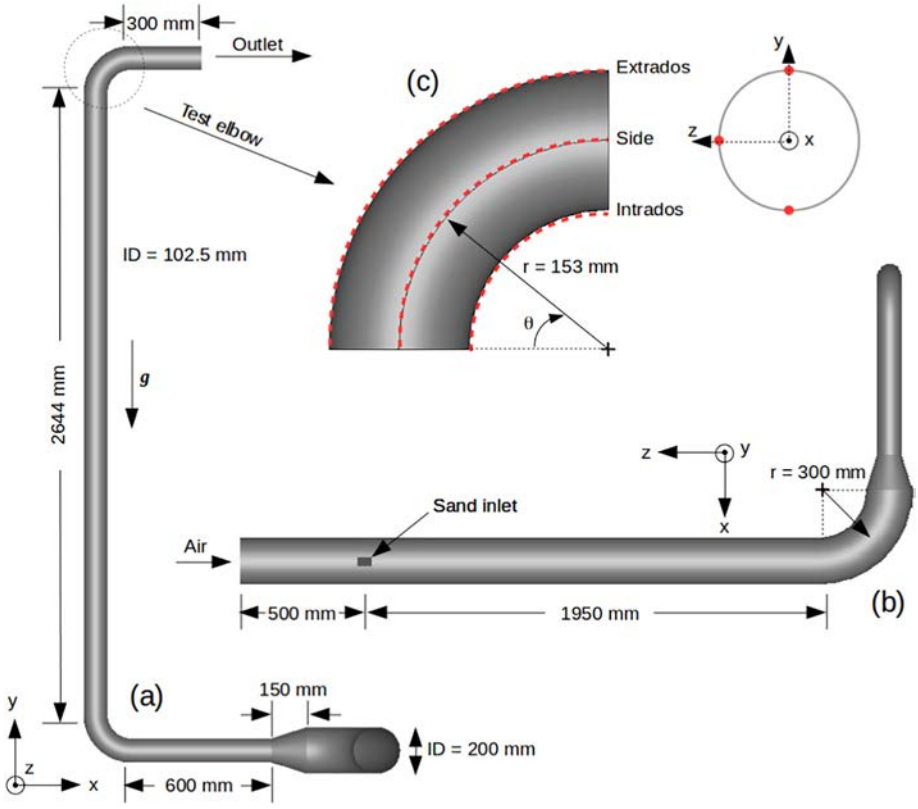

Fig. 1. Experimental set-up of Solnordal et al. [10]. (a) View in plane (*x*,*y*). (b) View in plane (*x*,*z*). (c) Zoom of test elbow. Red dashed lines and points correspond to extrados, side and intrados locations from different views, respectively.

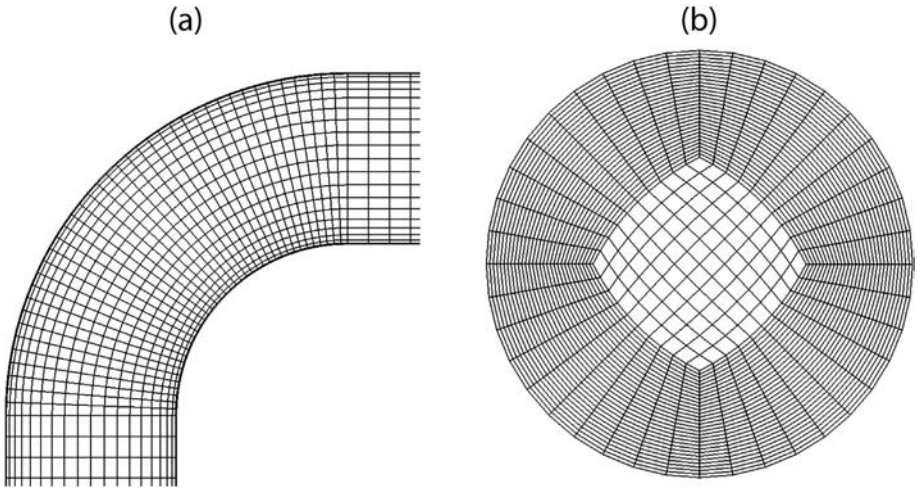

Fig. 2. (a) Surface mesh on test elbow. (b) Surface mesh of the cross-section.

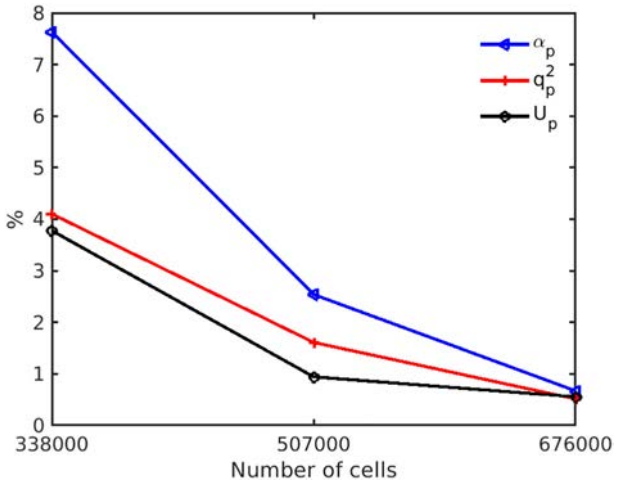

Fig. 3. Mesh independence study.

Table 1
Constants used in the erosion model of the present study. They are identical to those used by Solnordal et al. [10].

Constant	Value	Constant	Value
C	1.44×10^{8}	W	3.4
n	2.2	X	0.4
A	7	Y	0.9
B	5.45	Z	1.556056
		α_0	23°

Euler Euler model but approximated using the corresponding fluid quantity, which is a key physical parameter in their model.

In the present work, a CFD study on wall erosion in a 90° standard pipe elbow is performed using the NEPTUNE_CFD code [24]. A model is proposed to predict erosion rate based on an Euler Euler approach. The paper is organized as follows: Section 2 gives the numerical simulation details. The mathematical formulation of an erosion model which takes into account the particle turbulent kinetic energy is provided in Section 3. In Section 4, the results about the erosion spatial distributions are presented. Conclusions are drawn in Section 5.

2. Numerical simulation overview

2.1. System geometry

The configuration shown in Fig. 1 is essentially that used by Solnordal et al. [10] in their experiments. The orientation of gravity acceleration is $-y$. The last straight pipe at outlet is shortened from 1200 *mm* in Solnordal et al. [10] to 300 *mm*. It has been verified that this change does not affect in any way the gas solid flow in the elbow itself. Particles are injected at the same positions in the experiments and simulations. We took special care to impose the same solid mass flow rate although the inlet geometry is slightly different.

The whole pipe system consists of two parts: a section of large diameter pipe ($D = 200$ *mm*) close to inlet and a long section of small diameter pipe ($D = 102.5$ *mm*) which includes the test elbow. The two sections are connected by a reducer that is 150 *mm* in length, over which the average gas velocity would increase from 21.01 to 80 *m/s*. The test elbow is a standard 90° elbow with $r/D = 1.5$ (r is the radius of curvature).

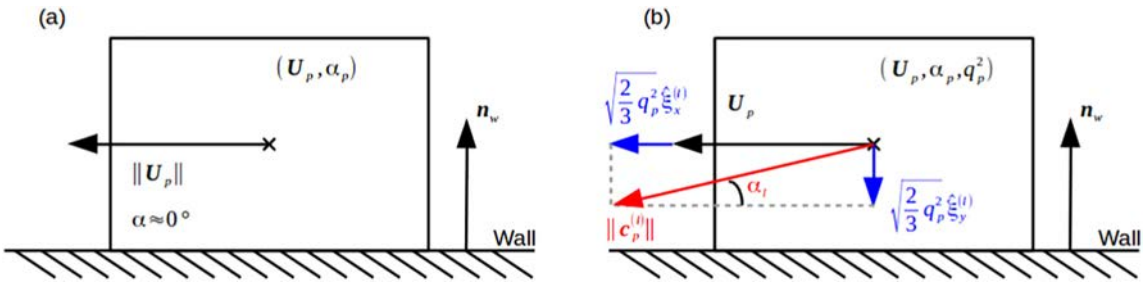

Fig. 4. Sketch of particle velocity in the first cell close to the wall. (a) Without any model. (b) Taking into account the particle turbulent kinetic energy q_p^2.

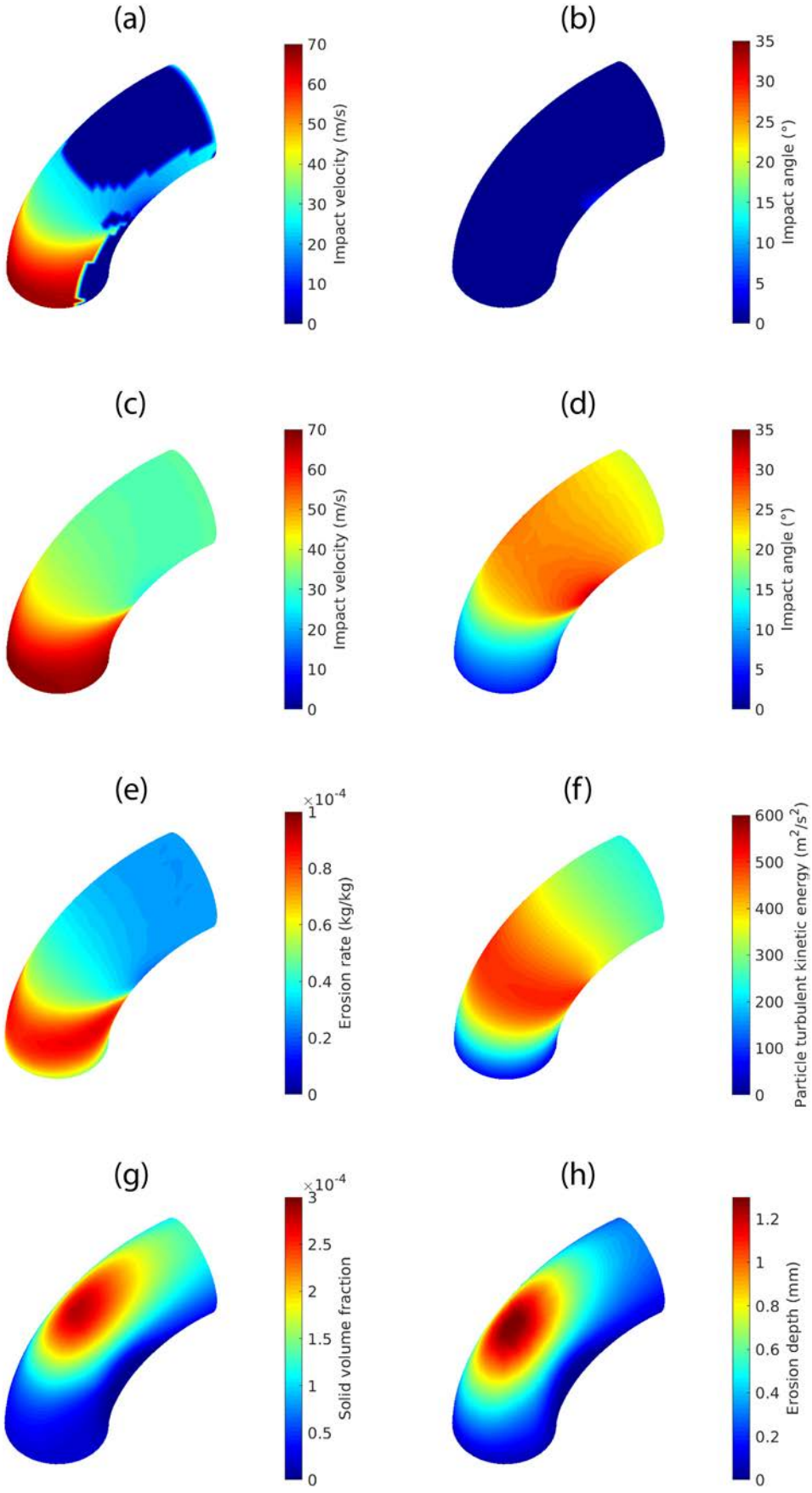

Fig. 5. Contours of erosion related quantities. (a) Impact velocity V_p without model of Section 3. (b) Impact angle α without model of Section 3. (c) Impact velocity $<V_p>$ with model of Section 3. (d) Impact angle $<\alpha>$ with model of Section 3. (e) Erosion rate $<\varepsilon>$ with model of Section 3. (f) Particle turbulent kinetic energy q_p^2. (g) Particle concentration α_p. (h) Erosion depth ε_H after passage of 200 *kg* sand.

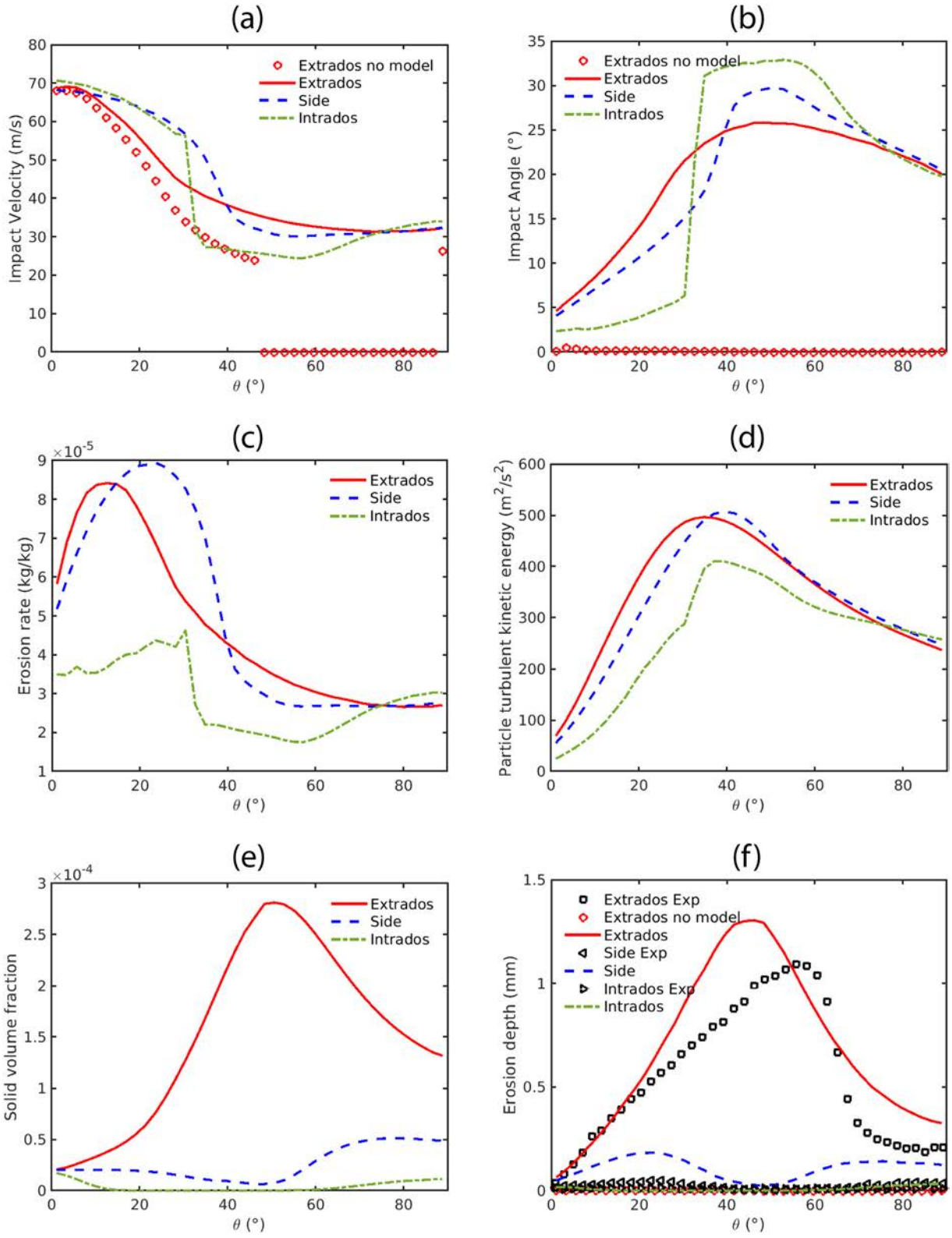

Fig. 6. Profiles of erosion related quantities along the elbow extrados, side and intrados. (a) Impact velocity. (b) Impact angle. (c) Erosion rate. (d) Particle turbulent kinetic energy q_p^2. (e) Particle concentration α_p. (f) Erosion depth ε_H after passage of 200 *kg* sand. "Exp" for experimental data of [10].

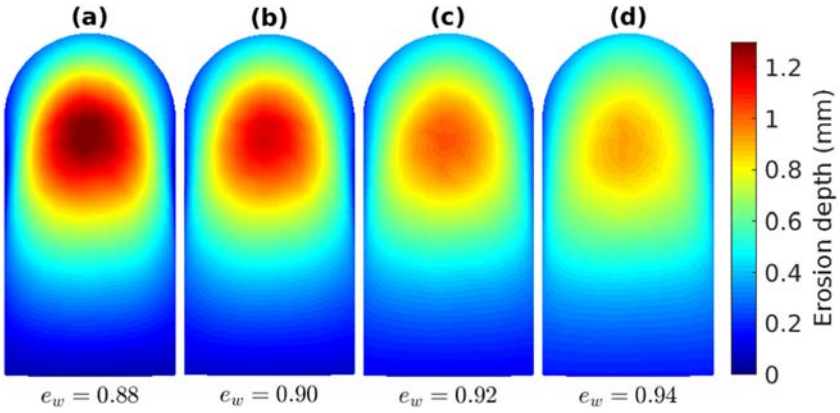

Fig. 7. Contours of erosion depth for different particle-wall restitution coefficients e_w in a view of the plane (y,z). (a) $e_w = 0.88$. (b) $e_w = 0.90$. (c) $e_w = 0.92$. (d) $e_w = 0.94$.

2.2. CFD code overview

Three dimensional numerical simulations are carried out using an Eulerian n fluid modelling approach for poly dispersed fluid particle flows implemented in NEPTUNE_CFD software which is developed by IMFT (Institut de Mécanique des Fluides de Toulouse). NEPTUNE_CFD is a multiphase flow code developed in the framework of the NEPTUNE project, financially supported by CEA (Commissariat à l'Énergie Atomique), EDF (Électricité de France), IRSN (Institut de Radioprotec tion et de Sûreté Nucléaire) and Framatome.

The multiphase Eulerian approach is derived from a joint fluid par ticle Probability Density Function (PDF) equation allowing one to derive transport equations for the mass, momentum and agitation of particle phases [25]. In the proposed modelling approach, transport equations (mass, momentum and fluctuating kinetic energy) are solved for each phase and coupled through interphase transfer terms. More details are found in Appendix A.

2.3. Numerical parameters

According to their experimental conditions [10], a uniform gas ve locity $V_{gas} = 21.01\ m/s$ is set at air inlet to generate a mass flow rate $\dot{m}_g$ $0.78\ kg/s$. The density and viscosity of air are $\rho_g = 1.18\ kg/m^3$ and μ_g $= 1.8 \times 10^{-5}\ kg/m/s$, respectively. A constant zero pressure is assumed for outlet boundary condition. A friction wall boundary condition is set for both phases and will be detailed in Section 4.2.

Experimental results after passage of 200 kg sand through the pipe system are selected to compare with our numerical prediction. The solid mass flow rate at sand inlet is $\dot{m}_p$ $0.03\ kg/s$ with a uniform inlet velocity of 1 m/s. The turbulence intensity is fixed to 0.6%. No sig nificant effect on the results is observed when increasing the turbulence intensity to 3%. An angular "70 Grade Sand" with a size distribution from 90 to 355 μm was used in the experiments of Solnordal et al. [10] (me dian diameter $d_{50} = 184\ \mu m$ and density $\rho_p = 2650\ kg/m^3$). It should be noted here that our numerical predictions of erosion depth were nearly identical for the runs where particles were assumed to be poly disperse and monodisperse. Therefore, in order to reduce the computa tional cost, one single particle size $d_p = 184\ \mu m$ was used for all the cases studied here.

Because of the large particle to gas density ratio, only the drag force is acting on the particles and the momentum transfer between the phases is modeled using the drag law of Wen and Yu [26]. It should be noted that the lift force acting on particles is not considered in our model. According to Duarte et al. [17], the Saffman lift force may play an important role in the particle spatial distribution across the pipe section, correspondingly the erosion spatial distribution. This would need further investigation which is out scope of this study (since a model of lift forces for dense suspensions does not exist).

The turbulence model $R_{ij} - \epsilon$ is chosen for the gas flow due to the high degree of anisotropy and significant streamline curvature occur ring in flows through the pipe bend. The particle agitation is obtained by solving two transport equations: one for the particle agitation and one for the fluid particle covariance. This includes the particle disper sion by the turbulence, and the inter particle collisions.

2.4. Computational mesh

Fig. 2 shows the surface mesh on the test elbow and the mesh in the cross section. A detailed sensitivity analysis to mesh properties has been carried out to determine the number of mesh cells close to the wall (20 cells) and to the center (10 cells) in the cross section, and the number of mesh cells in the straight pipe (80 cells for one meter long) and in the elbow (40 cells) in the direction of flow. Based on these recommendations, a reference mesh with 676,000 hexahedral cells is generated. In order to verify mesh independence, two coarser (338,000 and 507,000 cells) and one more refined (845,000 cells) meshes are generated by keeping the same first mesh cell size close to the wall ($y = 0.8\ mm$, corresponding to $y^+ = 107$ in wall units). Fig. 3 shows percentage difference for several physical quantities of par ticles at the curvature angle $\theta = 45^\circ$ on the extrados with each result compared to that obtained using the refined mesh (845,000 cells). The reference mesh (676,000 cells) provides relative differences that are re duced to less than 1% for the three key quantities required by the ero sion model. For this reason, the mesh with 676,000 cells has been selected as a good compromise on simulation accuracy and computa tional cost.

3. Erosion model based on Euler-Euler approach

The empirical erosion model proposed by Ahlert [27] used in the study of Solnordal et al. [10] is also chosen here. It can be expressed as

$$\varepsilon(\mathbf{u}_p) \quad C\mathbf{u}_p{}^n f(\alpha) f(\alpha) \begin{cases} A\alpha^2 + B\alpha & \alpha \le \alpha_0 \\ X\cos^2(\alpha)\sin(W\alpha) + Y\sin^2(\alpha) + Z & \alpha > \alpha_0 \end{cases} \tag{1}$$

where ε is the erosion rate at the wall (kg_t/kg_p, mass loss of target mate rial eroded by unit mass of solid particles), $\mathbf{u}_p$ is the instantaneous veloc ity of a particle impacting the wall with the impact angle α. The exponent n usually takes a value between 2 and 3 for ductile materials (Sheldon and Kanhere [28]), while C is a scaling parameter depending

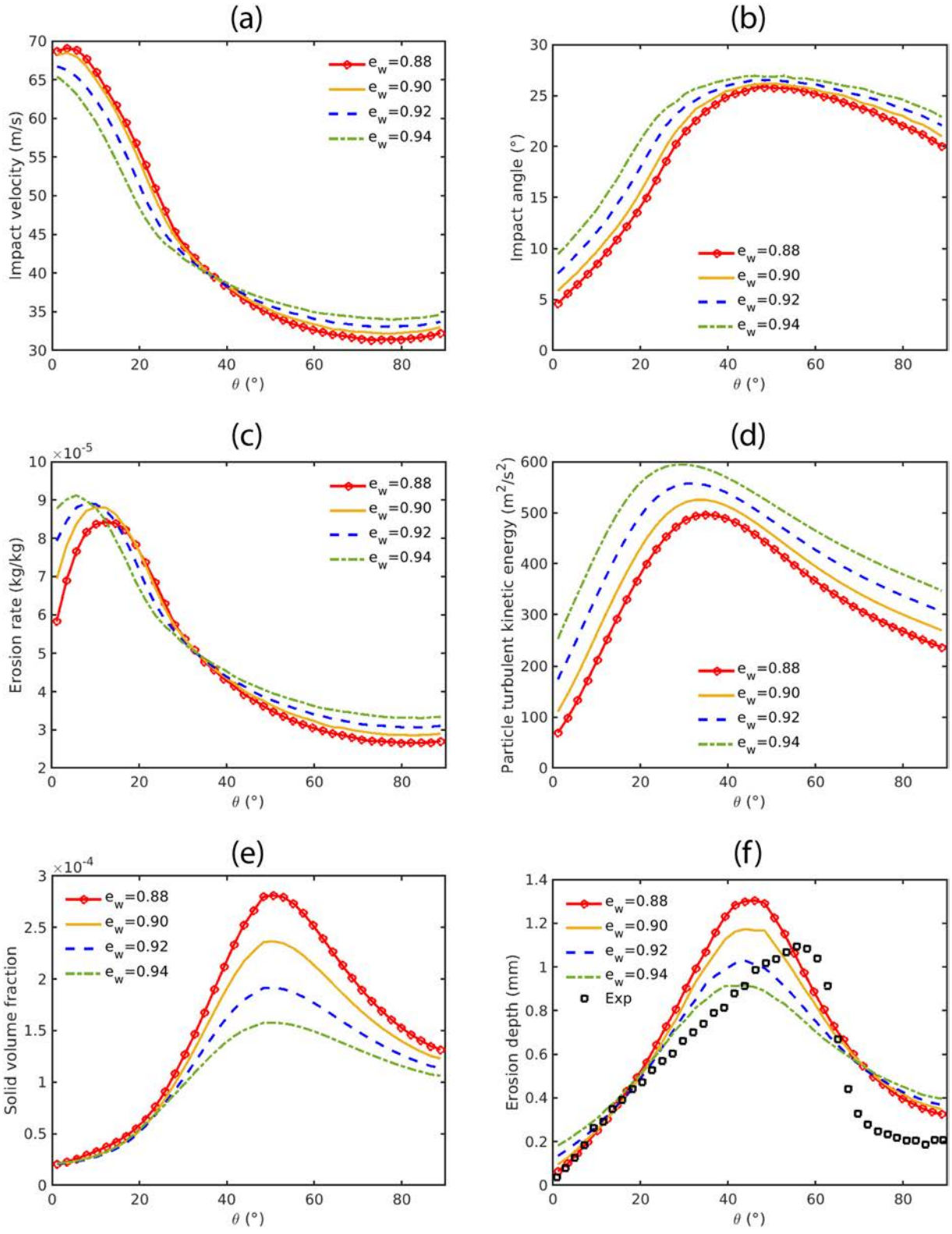

Fig. 8. Profiles of erosion related quantities along the elbow extrados for different particle-wall restitution coefficients e_w. (a) Impact velocity. (b) Impact angle. (c) Erosion rate. (d) Particle turbulent kinetic energy. (e) Particle concentration. (f) Erosion depth.

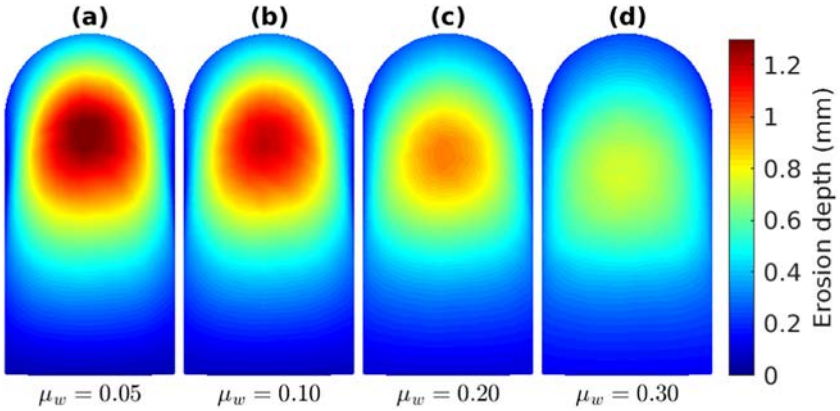

Fig. 9. Contours of erosion depth for different wall-normal dynamic friction coefficients μ_w in a view of the plane (y,z). (a) $\mu_w = 0.05$. (b) $\mu_w = 0.10$. (c) $\mu_w = 0.20$. (d) $\mu_w = 0.30$.

on particle size, shape, hardness, target properties etc. The function $f(\alpha)$ takes into account the impact angle effect on the erosion rate. The constants used in Eq. (1) are given in Table 1, these values were determined for angular sand particles impacting aluminum (*Al* grade 6061).

In order to compare with erosion depth measured in Solnordal et al. [10], a mass erosion rate ε_m is first derived to describe the mass loss of target material per unit area per second ($kg_t/m^2/s$). This is related to the empirical erosion rate ε and the particle flux towards the wall. Introducing the probability density function (pdf) $f(\mathbf{x},\mathbf{c}_p;t)$ which is defined such that $f(\mathbf{x},\mathbf{c}_p;t)d\mathbf{c}_p d\mathbf{x}$ is the mean probable number of particles with a centre of mass located in $[\mathbf{x},\mathbf{x}+d\mathbf{x}]$ with particle velocity in $[\mathbf{c}_p,\mathbf{c}_p+d\mathbf{c}_p]$, the particle flux towards the wall per unit area $\mathcal{F}$ ($kg_p/m^2/s$) can be express as

$$\mathcal{F} \quad \int_{\mathbf{c}_p\cdot\mathbf{n}_w<0} m_p\left[\mathbf{c}_p \quad \mathbf{n}_w\right] f(\mathbf{c}_p)\, d\mathbf{c}_p \tag{2}$$

where m_p is the mass of a single particle and $\mathbf{n}_w$ is the unit normal vector pointing from the wall towards the flow (see Fig. 4(a)).

Using eq:particleflux the mass erosion rate ε_m can be written as

$$\varepsilon_m \quad -\int_{\mathbf{c}_p\cdot\mathbf{n}_w<0} \varepsilon(\mathbf{c}_p) m_p\left[\mathbf{c}_p \quad \mathbf{n}_w\right] f(\mathbf{c}_p)\, d\mathbf{c}_p \tag{3}$$

where $\varepsilon(\mathbf{c}_p)$ is evaluated using eq:ahlert.

Now the depth erosion rate can be expressed as

$$\varepsilon_h \quad \frac{\varepsilon_m}{\rho_t} \tag{4}$$

where ε_h corresponds to the depth eroded per second by solid particles (m/s) and ρ_t is the density of the target material (kg/m^3). Erosion depth is the product of the depth erosion rate and the total time of the erosion test.

We must now comment on the method of determining the quantities needed in Eq. (3) or Eq. (4) from an Euler/Euler numerical simulation in which only the mean properties of the particles are known, such as the mean number density (or the solid volume fraction), the mean particle velocity and the mean particle kinetic energy. First, Eq. (3) is applied in each wall boundary cells of the Euler/Euler simulation. Also we assume that the dynamical properties of the particles are unchanged between the cell's centre and the real wall impact position, namely when the particle to wall distance equals one radius. Such an assumption allows us to use the variables of the wall boundary cells for computing Eq. (3).

Under these assumptions, for computing Eq. (3) it is necessary to estimate the instantaneous particle velocity that is required in the erosion rate model (in other words we have to prescribe the pdf shape). Assuming that the particle velocity distribution is Gaussian, the instantaneous particle velocity can be approximated as

$$c_{p,i} \quad U_{p,i} + \sqrt{\frac{2}{3}q_p^2}\ \ \hat{\xi}_i \tag{5}$$

where $U_{p,\,i}$ is the i^{th} component of the mean particle velocity and q_p^2 is the particle kinetic energy (both are obtained from the CFD simulations). $\hat{\xi}_i$ is a random number following a normalized Gaussian distribution. To compute the erosion rate, the pdf is sampled over a given number, N_{samp}, of instantaneous particle velocities constructed with Eq. (5). Hence Eq. (3) is computed as

$$\varepsilon_m \quad -\rho_p\alpha_p \frac{1}{N_{samp}} \sum_{l\ 1}^{N_{samp}} \varepsilon\left(c_p^{(l)}\right)\left[\mathbf{c}_p^{(l)} \quad \mathbf{n}_w\right] \quad \text{if} \quad \mathbf{c}_p^{(l)} \quad \mathbf{n}_w<0 \tag{6}$$

where $\mathbf{c}_p^{(l)}$ is generated with Eq. (5) and $\varepsilon(\mathbf{c}_p^{(l)})$ is calculated from Eq. (1). In Eq. (6) we used the relation $n_p m_p = \rho_p \alpha_p$, where α_p is the local particle volume fraction, which also comes from the simulations.

The number of samples is just a numerical parameter for approximating the integral in Eq. (3). Basically, the larger the number of samples is, the more accurate the approximation of the integral becomes. In the present study the number of samples has been set to 100,000 to achieve statistical convergence to the mean particle velocity and the mean particle kinetic energy computed from CFD simulations. As shown in Fig. 4 (b), the fluctuating part of particle velocity generates a deviation of impact direction to the wall which yields the erosion. This erosion model based on an Eulerian approach will be validated in Section 4.

4. Results

After the two validation cases presented in Appendix B were completed, the gas solid two phase flow simulations in a 90° standard pipe elbow were conducted using NEPTUNE_CFD. The detailed experiments of Solnordal et al. [10] are chosen to validate our erosion model based on Euler Euler approach. Then, the effects of particle wall boundary conditions, inlet solid mass flow rate ($\dot{m}_p$) and particle particle normal restitution coefficient (e_c) on erosion are investigated, respectively.

4.1. Erosion model based on Euler Euler approach

Figs. 5 and 6 show the important quantities in the erosion model that were extracted from our Euler Euler simulations.

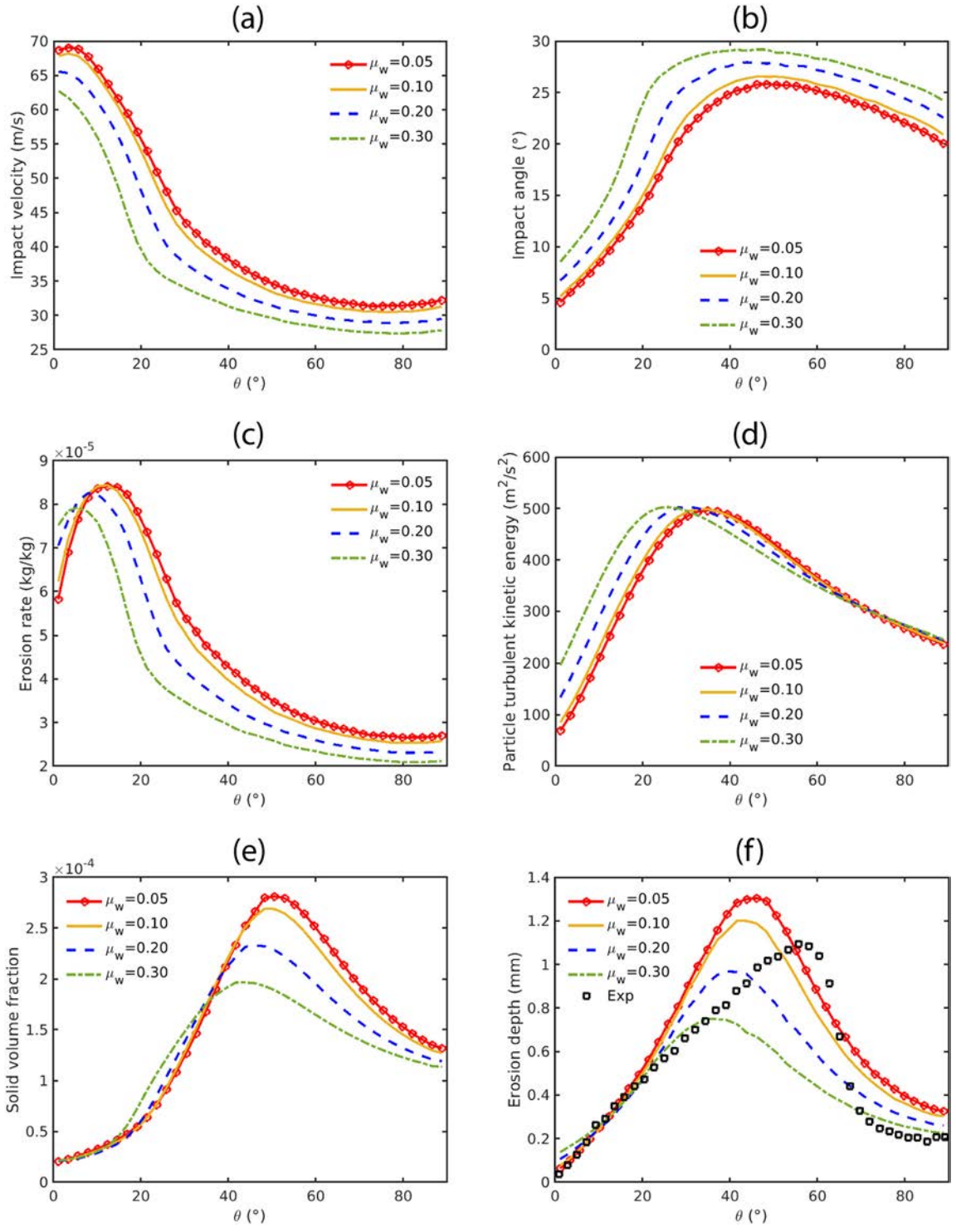

Fig. 10. Profiles of erosion related quantities along the elbow extrados for different wall-normal dynamic friction coefficients μ_w. (a) Impact velocity. (b) Impact angle. (c) Erosion rate. (d) Particle turbulent kinetic energy. (e) Particle concentration. (f) Erosion depth.

As shown by Fig. 4(a), if only considering particle velocity in the clos est cell to the elbow wall as the impact velocity, the impact angle would be nearly zero because the particle velocity is parallel to the wall with a slip particle boundary condition (see Fig. 5(b)). As shown by Fig. 5(a), the impact velocity is zero upstream of the inner surface and downstream of the outer surface of the elbow, meaning that no impact occurs in these regions because their velocity directions deviate only slightly from a di rection tangential to the wall and point towards the core of elbow. Conse quently, erosion depth would be predicted to be zero under this condition. Fig. 5(c) (h) show results with the application of the erosion model which takes into account the particle turbulent kinetic energy q_p^2. Fig. 5(f) shows that q_p^2 becomes significant over the entire elbow surface

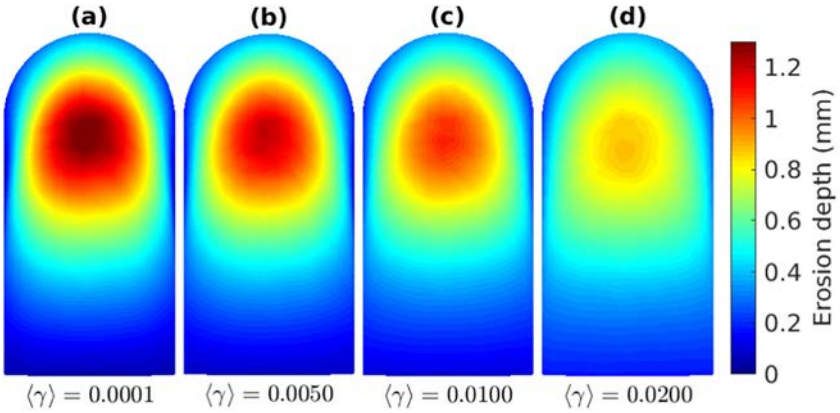

Fig. 11. Contours of erosion depth for different $\langle\gamma\rangle$ in a view of the plane (y,z). (a) $\langle\gamma\rangle = 0.0001$. (b) $\langle\gamma\rangle = 0.0050$. (c)$\langle\gamma\rangle = 0.0100$. (d) $\langle\gamma\rangle = 0.0200$.

especially in the region where the curvature angle θ varies between 30° and 50°. Comparing Fig. 5(b) and Fig. 5(d), impact angle predictions are improved and show reasonable values over the entire elbow surface. In Fig. 5(c), the impact velocity is also changed, especially for the zero value region observed in Fig. 5(a). The erosion rate is shown by Fig. 5 (e), with a maximum value close to the elbow entrance. It was expected that particles arriving with a high impact velocity and low impact angle will damage more efficiently this region. Fig. 5(g) shows the particle con centration contour at the elbow surface. An elliptical particle distribution region is observed in the region $45° < \theta < 65°$ with the peak value located at $\theta = 50°$. The erosion spatial distribution in Fig. 5(h) has a shape similar to experimental results of Solnordal et al. [10], only one elliptical erosion scar is observed with the main region corresponding to $35° < \theta < 55°$. In Eq. (6), erosion depth is actually a combination of four variables (c_p, α, ε and α_p). Therefore, the peak location of erosion depth is not coincident simply with the peak location of particle concentration, it is shifted al most 10° from the peak location of particle concentration.

To provide more quantitative comparisons, profiles of erosion related quantities along the elbow extrados, side and intrados are shown in Fig. 6. Fig. 6(a) shows that the impact velocity increases slightly in $20° < \theta < 50°$ due to the combined effects of relatively low particle velocity and strong particle turbulent kinetic energy in this region (see Fig. 6(d)). After $\theta >$ 50°, the impact velocity changes suddenly from zero to a reasonable value because of the deviation of particle velocity direction to the elbow wall because of the contribution of $\sqrt{2q_p^2/3}$. In Fig. 6(b), the impact angle on the extrados is significantly improved compared to the profile produced using no model. The impact angle profile at the extrados is now lower at the entrance and higher at the outlet of the elbow, where the largest impact angle is around $\theta = 50°$. Solid particles flow almost parallel to the flow direction at the entrance, which leads to a smaller impact angle in this region. The larger impact angle observed at the second half of elbow results from two mecha nisms: 1. solid particles with large inertia will keep straight trajecto ries until collision with the second half of elbow; 2. consecutive particle wall collisions. Consequently, in Fig. 6(c), erosion rate is high in the first half of elbow and low in the second half. Fig. 6(d) shows that the magnitudes of particle turbulent kinetic energy at the three locations are rather similar. This indicates that the particle fluctuations are almost homogeneous in the cross section for all θ. The profiles of erosion depth along the extrados, side and intrados in Fig. 6(f) are closely correlated to particle concentration profiles in Fig. 6(e), which indicates that the erosion depth is mainly related to the particle concentration in this case. Our results are in good agreement with the experimental data. The maximum erosion depth is slightly overestimated. More importantly, the shape of the erosion profiles along three different locations and the corresponding relation ship between them are very similar to the experimental data. The peak location is around $\theta = 45°$, which is 11° away from the experi mental peak location $\theta = 56°$. It should be mentioned here that the peak locations predicted by studies [10,17] based on Euler Lagrangian approach are also close to $\theta = 45°$. The discrepancy on the peak loca tion may suggest that it exists some additional physical mechanisms which are not considered in the modellings and simulations. In order to learn more about these effects, the particle wall boundary conditions are now varied.

4.2. Effect of particle wall boundary conditions on erosion

The smooth and rough wall boundary conditions are determined by four modelling parameters [29]: particle wall normal restitution coeffi cient (e_w), wall normal dynamic friction coefficient (μ_w) and two wall roughness coefficients ($\langle\gamma\rangle$ for the mean value and $\langle\gamma^2\rangle$ for the vari ance). For example, the free slip particle wall boundary condition is $e_w = 1, \mu_w = 0, \langle\gamma\rangle = 0$ and $\langle\gamma^2\rangle = 0$ if pure elastic frictionless rebound of spherical particles on a flat wall is assumed. As mentioned in Solnordal et al. [10] and Duarte et al. [17], it is important to state that the values for these four model parameters are based on a best fit to the experimental erosion data due to the lack of direct physical mea surements and the lack of information about gas solid flow characteris tics inside the elbow in the present experimental set up. It should be also noted that the values for these four parameters used in the follow ing sections are the typical values which are in the same range found in the experiments performed by Sommerfeld and Kussin [30].

4.2.1. Effect of particle wall restitution coefficient e_w on erosion

Fig. 7 shows contours of erosion depth for four different values of e_w, varied from 0.88 to 0.94, while other parameters and conditions are kept unchanged. We can observe that the magnitude of erosion depth decreases when e_w increases. In addition, erosion spatial distributions are quite similar, only the magnitude of erosion depth is changed.

Further more, profiles of erosion related quantities along the elbow extrados for different values of e_w are shown in Fig. 8. As e_w increases, particles lose less energy during particle wall collisions, resulting in an increase of particle turbulent kinetic energy along the extrados (see Fig. 8(d)). Higher particle turbulent kinetic energy disperses particles from the wall to the core, leading to the decrease of particle

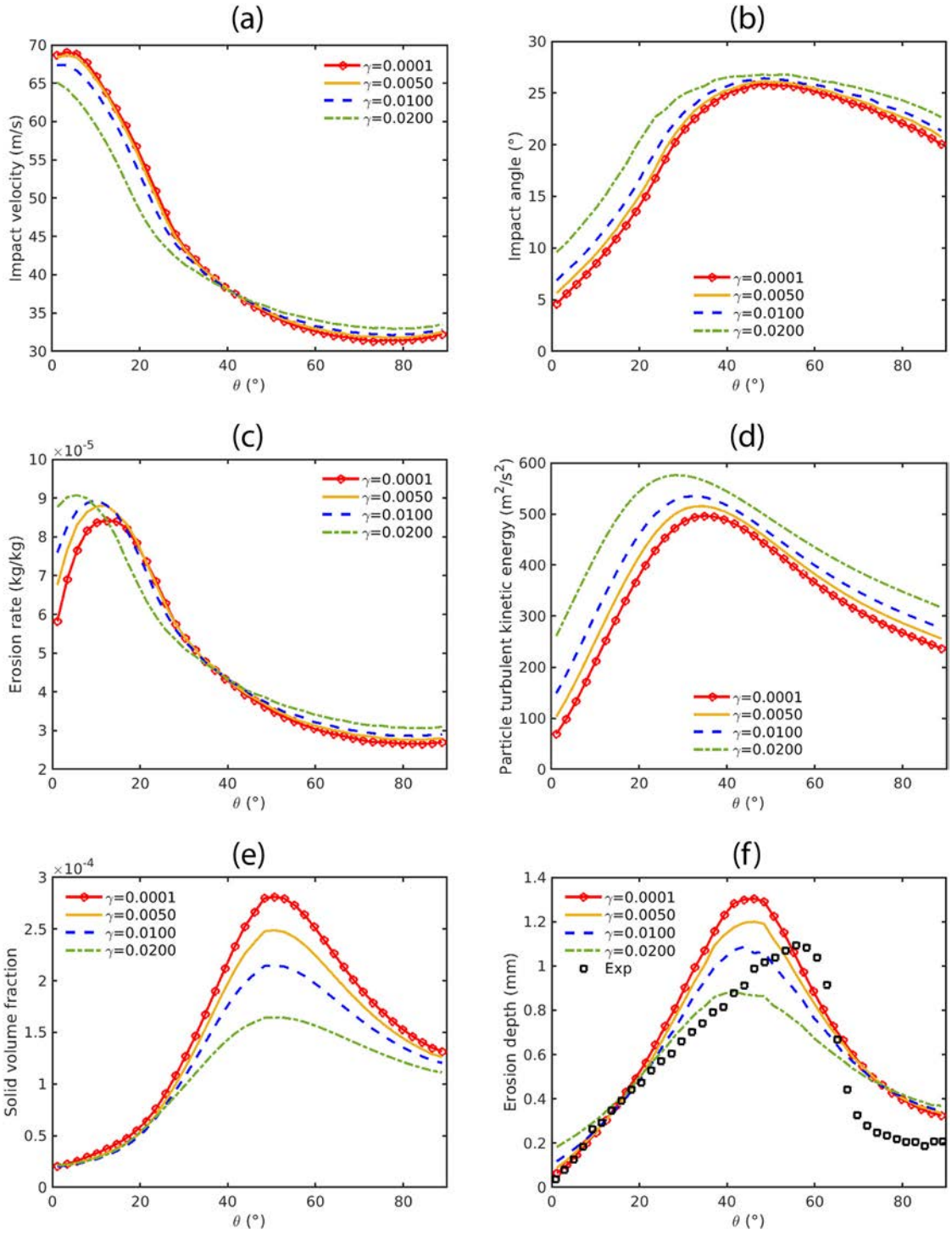

Fig. 12. Profiles of erosion related quantities along the elbow extrados for different $\langle\gamma\rangle$. (a) Impact velocity. (b) Impact angle. (c) Erosion rate. (d) Particle turbulent kinetic energy. (e) Particle concentration. (f) Erosion depth.

concentration along the extrados (see Fig. 8(e)). The modification of particle turbulent kinetic energy has also an effect on impact velocity and impact angle predicted from the erosion model. As shown in Fig. 8(a) and (b), impact velocity decreases on the first half of the extrados and increases on the second half, while impact angle increases along the whole extrados. In Fig. 8(c), erosion rate increases in the region close to the elbow entrance and outlet, which explains why erosion depth increases in these regions (see Fig. 8(f)). Erosion depth decreases close to the center of the extrados, which again is tightly correlated with particle concentration spatial distribution. It should be noted that erosion peak location does not change when varying e_w.

4.2.2. Effect of wall normal dynamic friction coefficient μ_w on erosion

Fig. 9 shows contours of erosion depth for four different values of μ_w varied from 0.05 to 0.30. This shows an effect opposite to that of e_w: erosion depth is reduced and erosion distribution changes at the same time

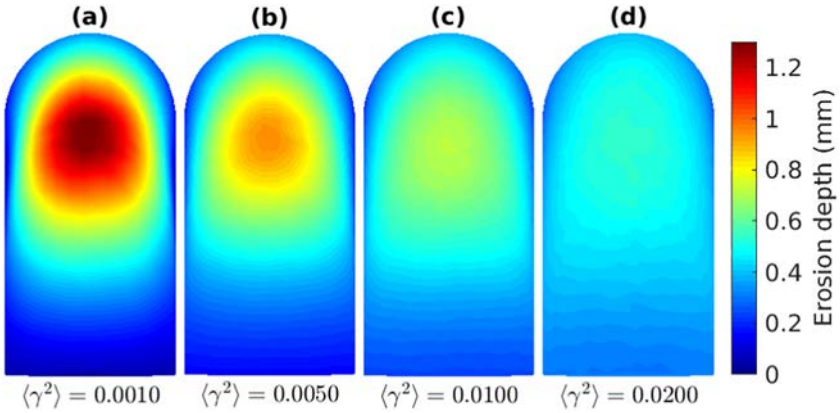

Fig. 13. Contours of erosion depth for different $\langle\gamma^2\rangle$ in a view of the plane (y,z). (a) $\langle\gamma^2\rangle = 0.0010$. (b) $\langle\gamma^2\rangle = 0.0050$. (c) $\langle\gamma^2\rangle = 0.0100$. (d) $\langle\gamma^2\rangle = 0.0200$.

and the erosion peak location moves slightly upstream when increasing μ_w.

Fig. 10 presents the profiles of erosion related quantities along the elbow extrados for different values of μ_w. In Fig. 10(d), it can be seen that particle turbulent kinetic energy is enhanced in the region $0^\circ < \theta < 30^\circ$, reduced for $30^\circ < \theta < 70^\circ$, and unchanged when $\theta > 70^\circ$. It seems that the maximum magnitude of particle turbulent kinetic energy on the extrados remains constant, only the location of the peak moves closer to the elbow entrance. Under the influence of wall friction, more particles are dispersed to the first half of the extrados, which increases the particle concentration in this region and also shifts its peak location from $\theta = 50^\circ$ to 45° (see Fig. 10(e)). Another effect of increasing μ_w is that particle velocity decreases along the entire extrados (see Fig. 10(a)). Lower particle velocity induces a higher impact angle for a given particle turbulent kinetic energy (see Fig. 10(b)). Consequently, erosion rate in Fig. 10(c) decreases when impact velocity decreases and impact angle increases. In Fig. 10(f), under the influence of the reduction of both the particle concentration and erosion rate, the erosion depth is reduced and its peak location is shifted from $\theta = 45^\circ$ to 35° (compared to the peak location 56° measured in the experiments of Solnordal et al. [10]).

4.2.3. Effect of roughness coefficients $\langle\gamma\rangle$ and $\langle\gamma^2\rangle$ on erosion

4.2.3.1. Mean of roughness distribution: $\langle\gamma\rangle$. Fig. 11 shows contours of erosion depth for four different values of $\langle\gamma\rangle$ varied from 0.0001 to 0.0200. Only the decrease of erosion depth is observed with increasing $\langle\gamma\rangle$; there is no effect on the peak location. A similar trend was observed as e_w was increased (see Figs. 7 and 11).

Profiles of erosion related quantities along the elbow extrados for different values of $\langle\gamma\rangle$ are shown in Fig. 12. It can be seen clearly that the increase of $\langle\gamma\rangle$ has similar effects on erosion related quantities as increasing e_w does. Erosion depth decreases because it is related to the reduction of particle concentration with peak still located at $\theta = 45^\circ$.

4.2.3.2. Variance of roughness distribution: $\langle\gamma^2\rangle$. Fig. 13 shows contours of erosion depth for four different values of $\langle\gamma^2\rangle$ varied from 0.0010 to 0.0200. Erosion depth is reduced obviously, especially in the case where $\langle\gamma^2\rangle = 0.0200$: at this condition, erosion is almost homogeneous on the outer surface of the elbow.

Profiles of erosion related quantities along the elbow extrados for different values of $\langle\gamma^2\rangle$ are shown in Fig. 14. Generally, the increase of $\langle\gamma^2\rangle$ yields the same trend as was observed with increasing $\langle\gamma\rangle$ but with a stronger effect. Taking the case $\langle\gamma\rangle = 0.0200$, $\langle\gamma^2\rangle = 0.0010$ (high mean roughness and negligible variance) in Fig. 11(d) and the case $\langle\gamma\rangle = 0.0001$, $\langle\gamma^2\rangle = 0.0200$ (negligible mean roughness with a strong variance) in Fig. 13(d) as examples, the contrast between these two cases signifies that erosion depth is more sensitive to higher variance than higher mean roughness.

4.3. Effect of inlet solid mass flow rate $\dot{m}_p$ on erosion

According to the previous studies mentioned in Section 1, opposite effects of inlet solid mass flow rate on erosion have been observed by Duarte et al. [9] (shielding effect that reduces erosion) and Xu et al. [12] (sliding effect that accelerates erosion). In order to provide new insight into this subject, the effect of inlet solid mass flow rate is also investigated ranging from $\dot{m}_p$ 0.03 to 1.92 *kg/s*. Here, we benefit from using the Euler Euler approach, which has a natural advantage for investigating conditions where particle concentrations are relatively high.

Fig. 15 shows contours of erosion depth after the passage of 200 *kg* sand with $\dot{m}_p$ varied from 0.03 to 1.92 *kg/s* while other parameters and conditions are kept fixed to the reference case. With the increase of inlet solid mass flow rate $\dot{m}_p$, both the magnitude and the form of erosion spatial distribution are clearly changed, as shown in Fig. 15. It seems that erosion depth increases with increasing $\dot{m}_p$. For the reference case ($\dot{m}_p$ 0.03 *kg/s*), erosion spatial distribution has an elliptical form that is nearly symmetrical along the extrados. From $\dot{m}_p$ 0.06 to 0.48 *kg/s*, the distribution is still symmetrical but the downstream part becomes sharper. With further increase in $\dot{m}_p$ from 0.96 to 1.92 *kg/s*, the erosion distribution along the extrados is no longer symmetrical.

Contours of particle turbulent kinetic energy for different values of $\dot{m}_p$ are presented in Fig. 16. Particle turbulent kinetic energy reduces progressively from both inlet and outlet of elbow for $\dot{m}_p$ varied from 0.03 to 0.24 *kg/s*; however it is still roughly homogeneous in each cross section. Then from $\dot{m}_p$ 0.48 to 1.92 *kg/s*, the homogeneous distribution for each θ disappears, a higher q_p^2 persists on both sides of the elbow, and lower q_p^2 is observed around the region near the extrados. This leads to a high particle concentration in this region of low q_p^2 (see Fig. 17(e), (f) and (g)). For $\dot{m}_p$ from 0.96 to 1.92 *kg/s*, particle turbulent kinetic energy (Fig. 16(f), (g)) and particle concentration (Fig. 17(f), (g)) are no longer symmetrical along the extrados. This is why the asymmetrical erosion spatial distribution of Fig. 15(f), (g) is observed. The cause of the asymmetry observed with high inlet solid mass flow rate is related to the geometry of the pipe and the presence of successive elbows with different orientations. Comparing two different inlet mass flow rates $\dot{m}_p$ 0.03 and 1.92 *kg/s* for example, the solid volume fraction at the entrance of the long vertical pipe is evidently inhomogeneous (see graphical abstract) after passing through the two pipe elbows of different orientations. In the dilute case $\dot{m}_p$ 0.03 *kg/s*, the

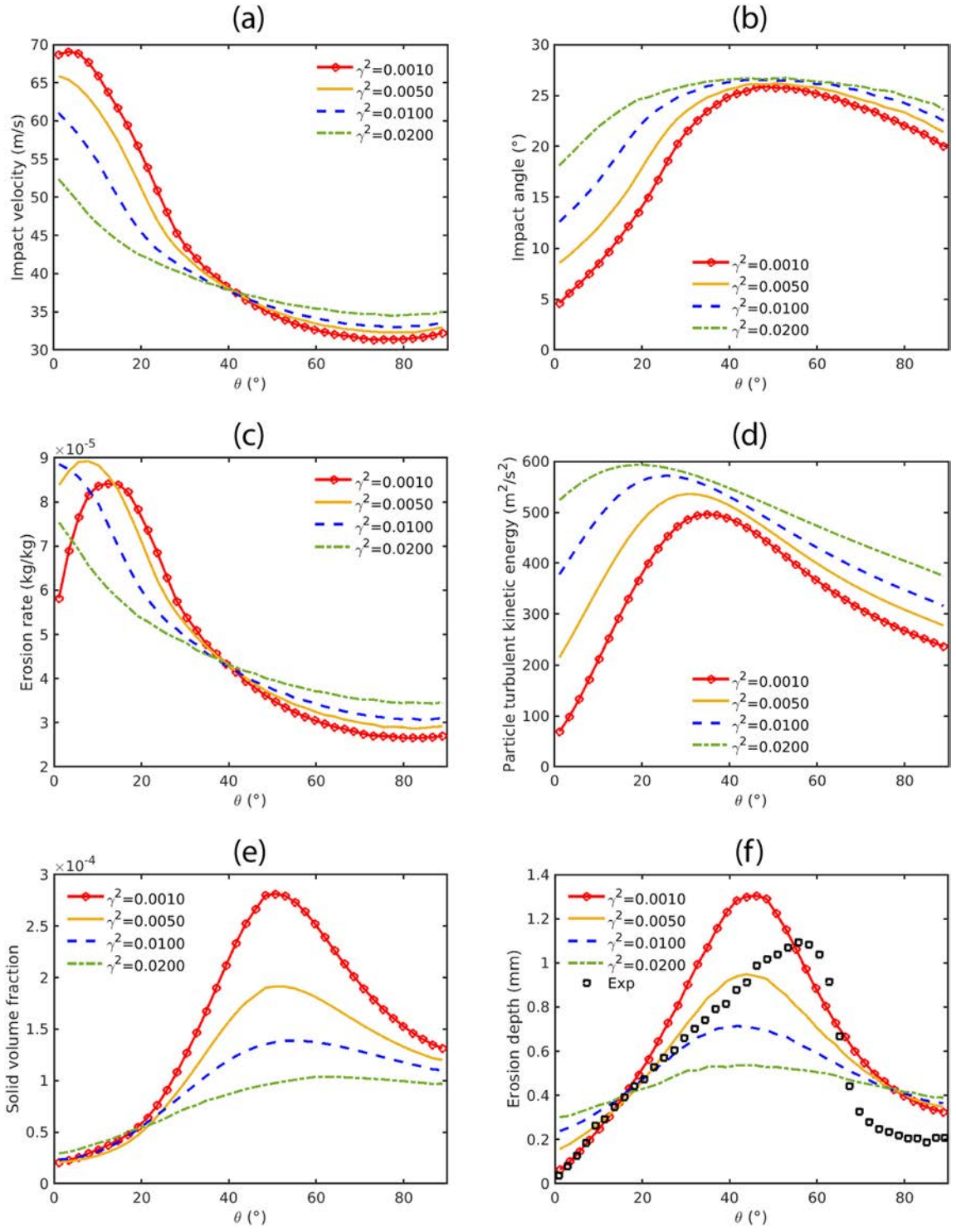

Fig. 14. Profiles of erosion related quantities along the elbow extrados for different $\langle\gamma^2\rangle$. (a) Impact velocity. (b) Impact angle. (c) Erosion rate. (d) Particle turbulent kinetic energy. (e) Particle concentration. (f) Erosion depth.

solid volume fraction becomes progressively more homogeneous up stream of the test elbow. However, in the case $\dot{m}_p$ 1.92 kg/s, en hanced inertia due to high inlet solid mass flow rate prevents redistribution of particles before impacting the test elbow. The peak of solid volume fraction rotates counterclockwise along the vertical pipe wall. This inhomogeneous distribution of particles at the section up stream of the test elbow is the main reason for the asymmetry of the erosion spatial distribution observed in Fig. 15.

Profiles of erosion related quantities along the elbow extrados for different values of $\dot{m}_p$ are shown in Fig. 18. In Fig. 18(a), impact velocity

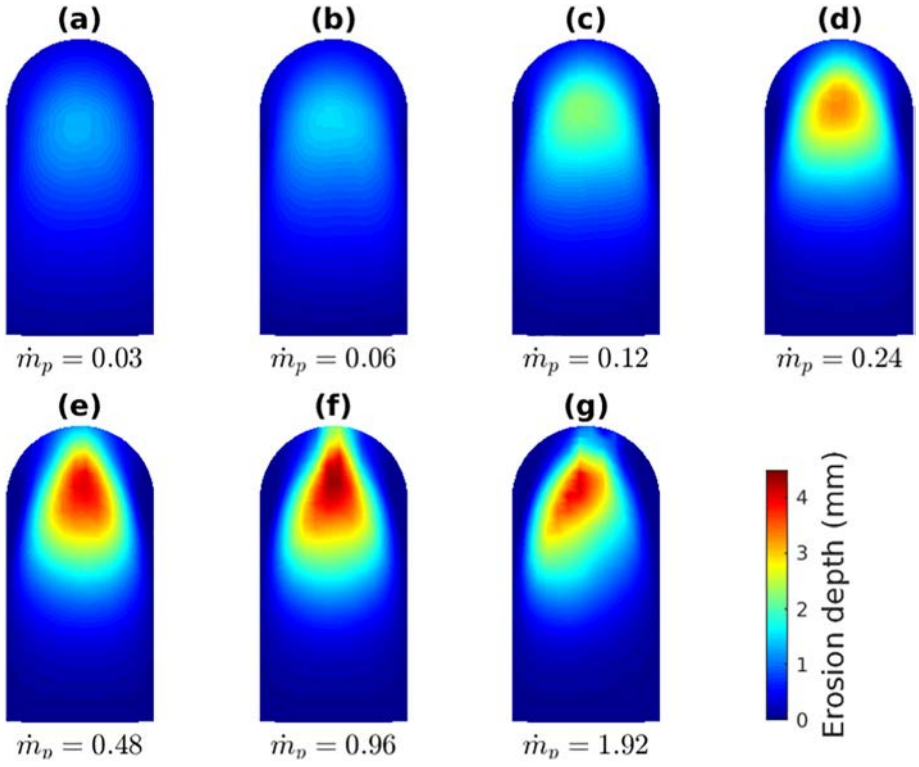

Fig. 15. Contours of erosion depth for different inlet solid mass flow rates m_p in a view of the plane (y,z). (a) m_p 0.03. (b) m_p 0.06. (c) m_p 0.12. (d) m_p 0.24. (e) m_p 0.48. (f) m_p 0.96. (g) m_p 1.92 kg/s.

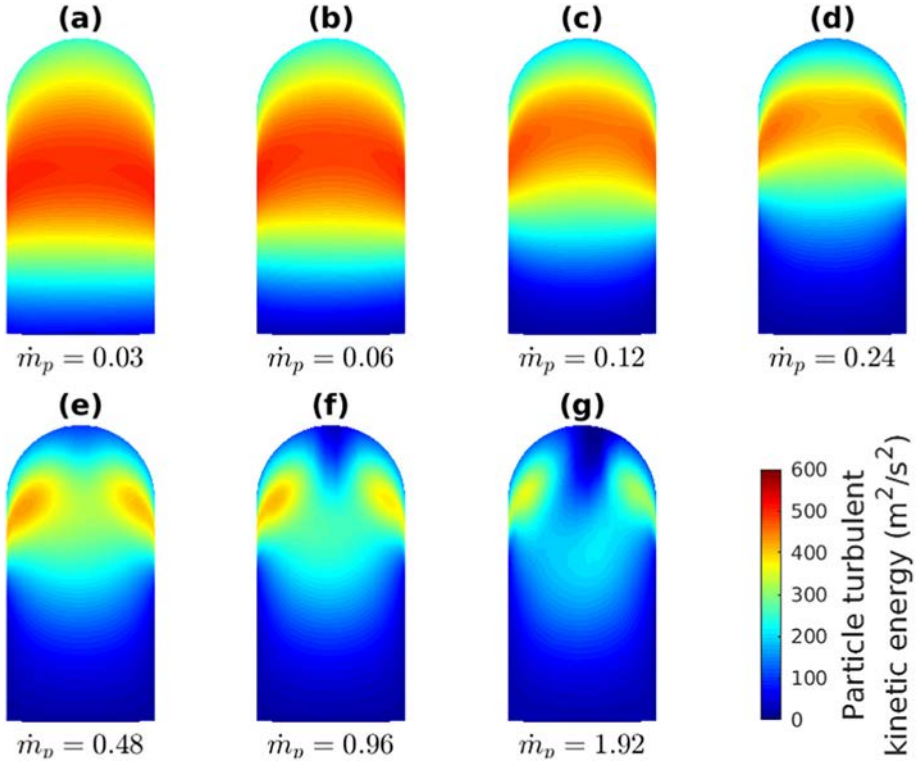

Fig. 16. Contours of particle turbulent kinetic energy for different inlet solid mass flow rates m_p in a view of the plane (y,z). (a) m_p 0.03. (b) m_p 0.06. (c) m_p 0.12. (d) m_p 0.24. (e) m_p 0.48. (f) m_p 0.96. (g) m_p 1.92 kg/s.

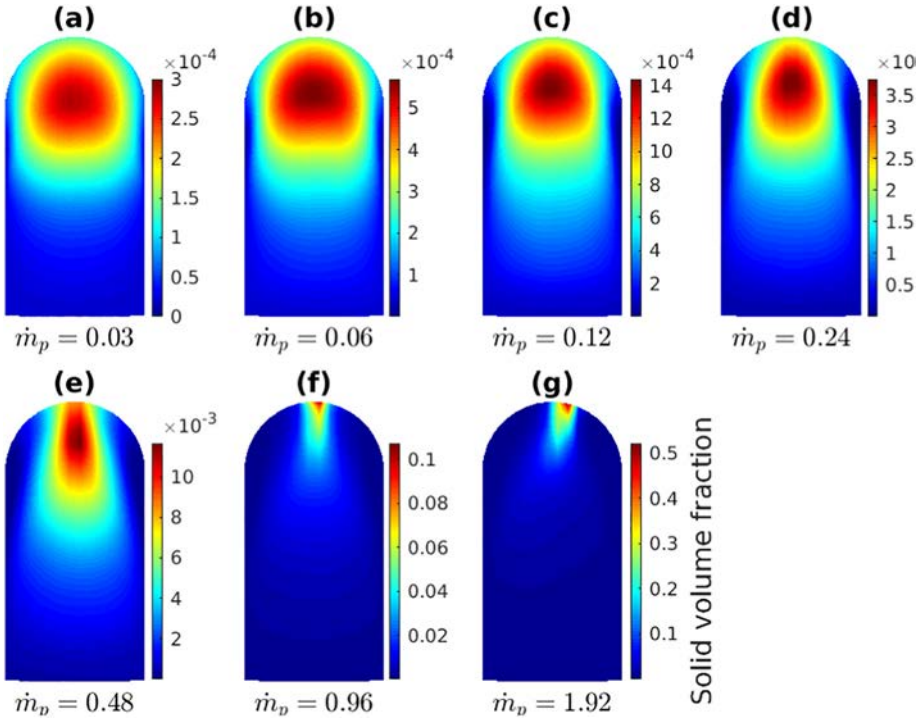

Fig. 17. Contours of particle concentration for different inlet solid mass flow rates m_p in a view of the plane (y,z). (a) m_p 0.03. (b) m_p 0.06. (c) m_p 0.12. (d) m_p 0.24. (e) m_p 0.48. (f) m_p 0.96. (g) m_p 1.92 kg/s.

increases first for $\dot{m}_p$ ranging from 0.03 to 0.48 kg/s, then it does not change as $\dot{m}_p$ is increased to 1.92 kg/s. In Fig. 18(b), impact angle de creases progressively with increasing $\dot{m}_p$, and is lower than 10° along the entire extrados for $\dot{m}_p$ 1.92 kg/s. Particle concentration under this condition is so high that particles can no longer impact directly the elbow surface; instead a layer of particles may form in the region near the extrados, then slides towards the elbow outlet, resulting in a low impact angle. Erosion rate increases first from 0.03 to 0.24 kg/s and then decreases from 0.48 to 1.92 kg/s for $\theta > 20°$ (see Fig. 18(c)). In Fig. 18(e), particle concentration has a peak value for $\dot{m}_p$ in the range 0.03 to 0.48 kg/s. For the cases $\dot{m}_p$ 0.96 and 1.92 kg/s, the peak disappears and the maximum particle concentration is located at the elbow outlet. In Fig. 18(f), erosion depth increases when $\dot{m}_p$ varies from 0.03 to 0.96 kg/s, then decreases from 0.96 to 1.92 kg/s, which is contrary to the observation of Duarte et al. [17], where it was observed that erosion depth decreases with increasing mass loading.

To compare these results more clearly, a dimensionless number to describe erosion efficiency is defined by

$$\frac{\dot{m}_{loss}}{\dot{m}_p} \tag{7}$$

where $\dot{m}_{loss}$ describes the total mass loss rate (dividing the total mass loss after the passage of 200 kg sand by the erosion test time). This di mensionless number is plotted as a function of $\dot{m}_p$, as shown in Fig. 19, with $\dot{m}_p$ varying from 0.0075 to 1.92 kg/s. Under dilute conditions, an increase of $\dot{m}_p$ would lead to a linear increase of $\dot{m}_{loss}$ by considering that the particle dynamics are not disturbed in dilute regime, which would correspond to a constant erosion efficiency number $\dot{m}_{loss}/\dot{m}_p$. Such a trend is observed in Fig. 19 for $\dot{m}_p$ from 0.0075 to 0.03 kg/s. Con tinuing to increase $\dot{m}_p$, particle concentration in the test elbow in creases, and when a threshold is exceeded, particle velocity and its impact angle change progressively as already observed in Fig. 18(a) and Fig. 18(b). Consequently, erosion efficiency number does not re main constant but increases for $\dot{m}_p$ from 0.06 to 0.96 kg/s. If we con tinue to increase $\dot{m}_p$ from 0.96 to 1.92 kg/s, solid concentration close to the elbow wall becomes extremely high, and erosion efficiency num ber $\dot{m}_{loss}/\dot{m}_p$ begins to decrease. It should be noted that the location of the maximum erosion depth changes also from $\theta = 45°$ to 55° as $\dot{m}_p$ is increased to 0.24 kg/s, then remains unchanged for further increases in $\dot{m}_p$.

Assuming that a certain amount of sand passes through the pipe elbow, according to Fig. 19, there exists a solid mass flow rate that is most efficient to erode the elbow wall ($\dot{m}_p$ 0.96 kg/s for the cases studied here), which should be avoided in pneumatic conveying pro cesses. One possible explanation for three stages observed in Fig. 19 is: i) In the dilute regime, when increasing $\dot{m}_p$, particle dynamics do not change significantly, meaning that each single particle would still im pact the elbow wall, so erosion efficiency is the same. ii) Continuing to increase $\dot{m}_p$, particle particle interactions start to become important. In the near wall region, it increases perhaps the particle wall collision frequency when a particle passes through the pipe elbow (for example, a particle would impact the wall 3 or 4 times comparing to 1 or 2 times in the dilute regime before leaving the elbow). Increased particle wall collision frequency may be the reason that erosion efficiency increases with $\dot{m}_p$. iii) Further increasing $\dot{m}_p$, particle particle collisions dominate in the elbow and these will dissipate more energy. Meanwhile, particles are likely to slide along the elbow surface instead impacting directly on it. In addition, not all the particles would impact the wall before leaving the elbow. As a result, the erosion efficiency begins to decrease.

4.4. Effect of particle particle interaction e_c on erosion

Due to the low particle concentration ($\alpha_{p\ max} = 2.8 \times 10^{-4}$) with $\dot{m}_p$ 0.03 kg/s, particle particle interactions are negligible in the refer ence case. In order to investigate the effect of e_c, $\dot{m}_p$ 0.96 kg/s is set

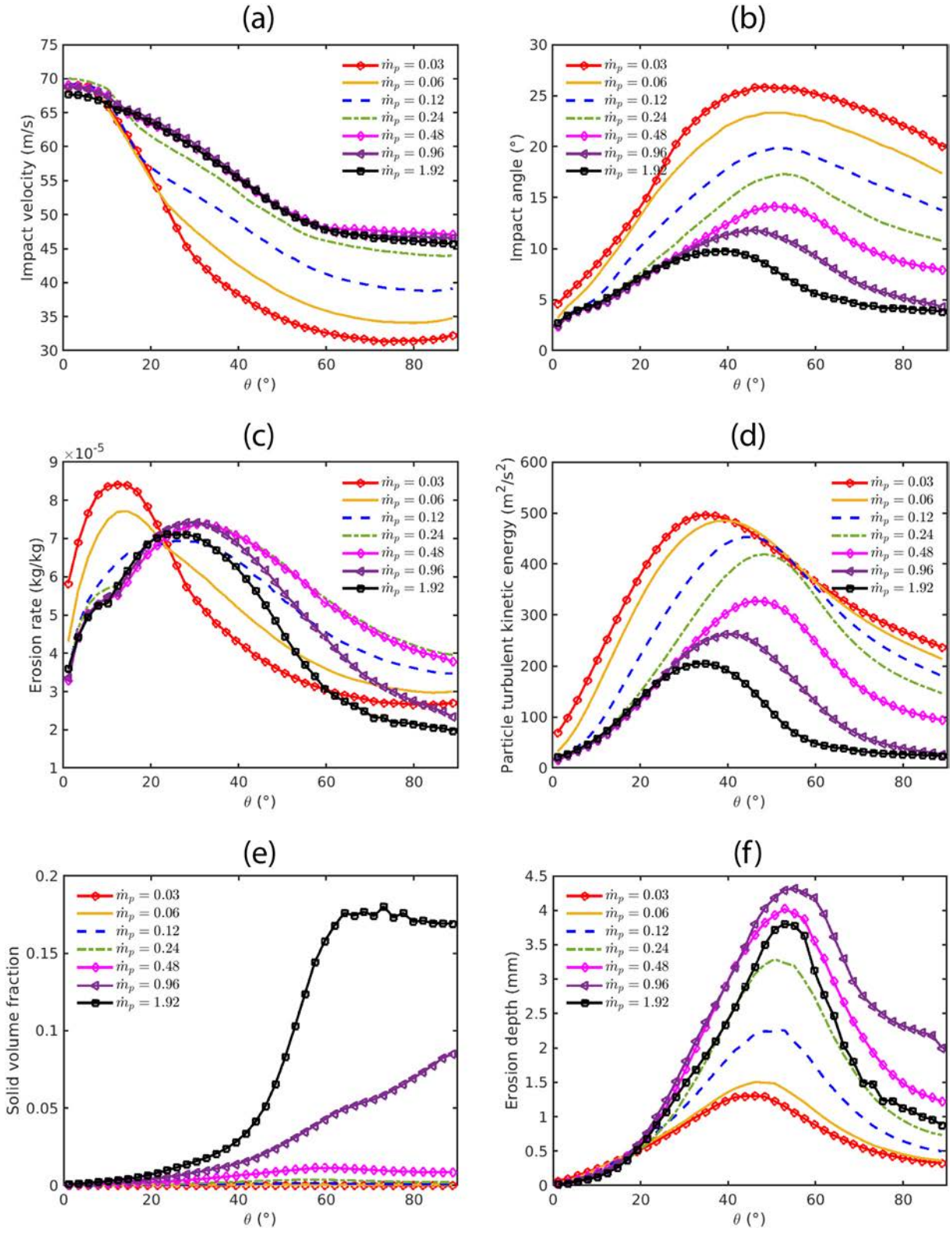

Fig. 18. Profiles of erosion related quantities along the elbow extrados for different inlet solid mass flow rates m_p. (a) Impact velocity. (b) Impact angle. (c) Erosion rate. (d) Particle turbulent kinetic energy. (e) Particle concentration. (f) Erosion depth.

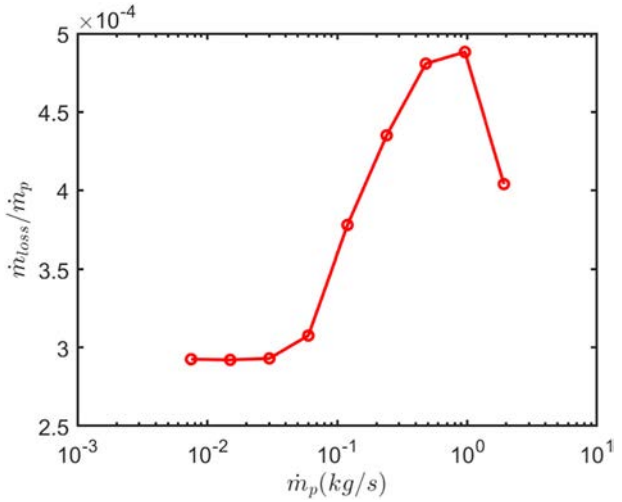

Fig. 19. Ratio between the total mass loss rate due to erosion and inlet solid mass flow rate m_p as a function of m_p.

for all four cases presented in Fig. 20, where contours of erosion depth for four different values of e_c varied from 0.90 to 0.96 are shown. The particle particle restitution coefficient models energy loss during parti cle particle collisions ($e_c = 1.0$ corresponds to an elastic collision; lower e_c corresponds to more energy lost by collisions). Variation of e_c weakly affects the magnitude of the erosion depth; however, the erosion distri bution is changed slightly from an asymmetrical to symmetrical form, which is related to particle dispersion effects.

More information about the variation of erosion related quantities along the elbow extrados is given in Fig. 21. It can be seen that all quan tities remain almost unchanged for $\theta < 40^{\circ}$ where particle concentration is less than 1%. In this region, collision frequency between particles is low so that particle velocity and concentration do not change much when varying e_c. However, the effect of e_c becomes more pronounced in the second half close to elbow outlet. Particle turbulent kinetic energy increases, particle concentration decreases and particles are dispersed towards the core of the elbow (see Fig. 21(d) and (e)). In Fig. 21(a), it can be seen that particle velocity does not change much. Therefore, the increase of impact angle and erosion rate is basically related to the increase of particle turbulence kinetic energy (see Fig. 21(b) and (c)). Fig. 21(f) shows that the peak location of erosion depth moves slightly upstream but its magnitude is constant. Erosion depth at the elbow outlet decreases because of the decrease of particle concentration in this region.

5. Conclusion

A CFD study on particle impact erosion in a 90° standard elbow is performed using the NEPTUNE_CFD code. A model based on the Euler Euler approach is proposed and validated for erosion prediction. The ef fects of particle wall normal restitution coefficient, wall normal dy namic friction coefficient, wall roughness coefficients, inlet solid mass flow rate and particle particle normal restitution coefficient on erosion depth and erosion spatial distribution are then investigated.

Particle wall boundary condition coefficients e_w, μ_w, $\langle\gamma\rangle$ and $\langle\gamma^2\rangle$ play an important role by redistributing particles in the region close to the wall. In general, the increase of e_w, $\langle\gamma\rangle$ and $\langle\gamma^2\rangle$ have similar effects: 1. The increase of particle turbulent kinetic energy on the whole elbow surface. 2. The decrease of particle concentration due to the dispersion of particles towards the core of the elbow. It should be noted that the maximum erosion location does not change when varying these three parameters. This is not the case for μ_w. The increase of μ_w does not change the magnitude of particle turbulent kinetic energy, but its peak moves upstream, followed by redistributing particles upstream of the elbow. Therefore, maximum erosion depth decreases and its location moves upstream.

Hence, these parameters are not determinant to leading order on the discrepancy of the peak location between the numerical prediction and the experimental results mentioned in Section 4.1. The normal contri bution of the particle kinetic energy is approximated by $\langle u_n' u_n' \rangle \approx 2/3 q_p^2$. In the near wall region, the particle kinetic stress tensor is strongly anisotropic and the assumption $\langle u_n' u_n' \rangle \approx 2/3 q_p^2$ may overestimate the friction at the wall. According to the analysis on the effect of particle wall dynamic friction coefficient μ_w, increasing the friction may shift the peak location upstream. Therefore, an anisotropic particle turbu lence model is likely to improve the prediction of peak location com pared to experimental results. This needs to be further investigated.

As the inlet solid mass flow rate increases, erosion efficiency stays nearly constant in the dilute regime, then increases with the inlet solid mass flow rate. At some limiting (high) value of inlet solid mass flow rate, the erosion efficiency begins to decrease. For a certain amount of sand passing through a pipe elbow, there exists a solid mass flow rate for which elbow damage is the most dramatic ($\dot{m}_p$ 0.96 kg/s in the configuration studied here).

As mentioned in Section 1, a “rabbit head” shaped erosion spatial distribution on the outer surface of the elbow has been observed in

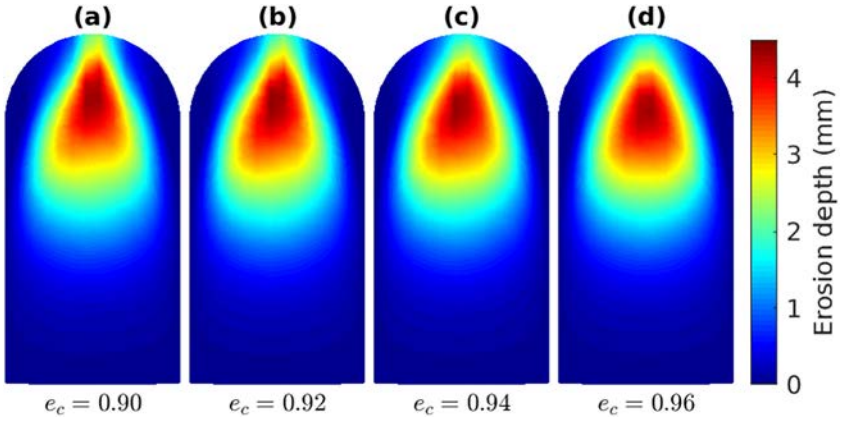

Fig. 20. Contours of erosion depth for different particle-particle restitution coefficients e_c for m_p 0.96 kg/s in a view of the plane (y,z). (a) $e_c = 0.90$. (b) $e_c = 0.92$. (c) $e_c = 0.94$. (d) $e_c = 0.96$.

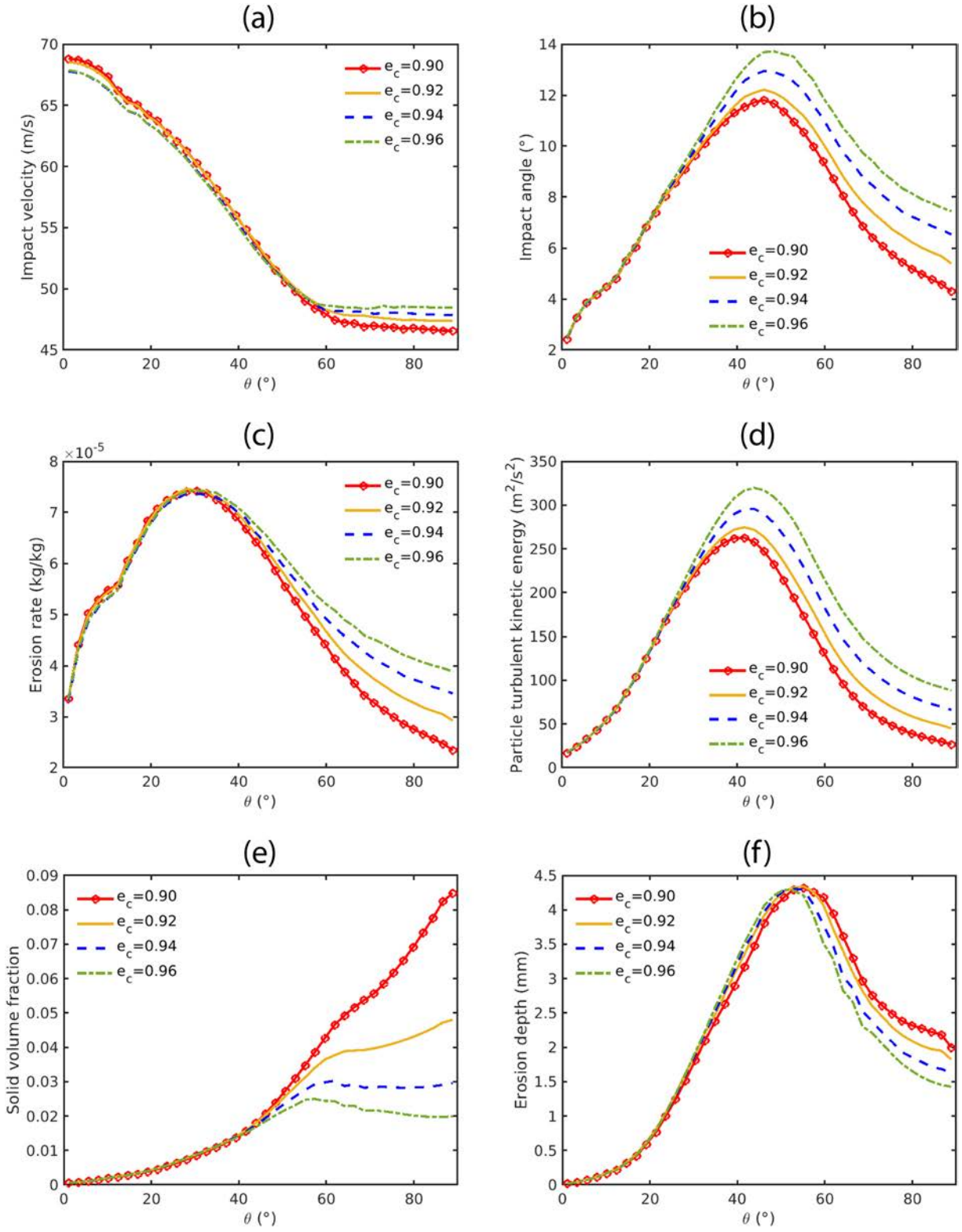

Fig. 21. Profiles of erosion related quantities along the elbow extrados for different particle-particle restitution coefficients e_c for m_p 0.96 kg/s. (a) Impact velocity. (b) Impact angle. (c) Erosion rate. (d) Particle turbulent kinetic energy. (e) Particle concentration. (f) Erosion depth.

many studies. This erosion spatial distribution does not occur in our simulations, not only for the cases presented here with the rough boundary conditions, but also for the cases with smooth boundary con ditions. According to the erosion model, erosion spatial distribution is conditioned by the particle concentration, which is the main reason why no secondary erosion regions are observed here.

Nomenclature

Latin symbols

$\mathbf{n}_w$	Unit normal vector to the wall $(-)$
$\mathbf{U}_p$	Mean particle velocity vector (m/s)
$\dot{m}_p$	Mass flow rate of solid particles impacting the wall (kg/s)
$\|\mathbf{u}_p\|$	Impact velocity of solid particles (m/s)
C	Constant in erosion model $(-)$
D	Diameter of the pipe (m)
d_p	Particle diameter (m)
d_{50}	Median diameter of sand particles (m)
d_{inlet}	Diameter of sand injection section (m)
e_c	Particle particle normal restitution coefficient $(-)$
e_w	Particle wall normal restitution coefficient $(-)$
$f(\alpha)$	Function of the impact angle in erosion model $(-)$
n	Exponent of impact velocity in erosion model $(-)$
N_{samp}	Number of samples following normal distribution $(-)$
q_p^2	Turbulent kinetic energy of solid particles (m^2/s^2)
q_{fp}	Covariance of gas and solid fluctuation velocity (m^2/s^2)
r	Radius of the bend (m)
R_{ij}	Reynolds stress (m^2/s^2)
V_{gas}	Gas velocity (m/s)

Greek symbols

α	Impact angle $(^\circ)$
α_p	Local solid volume fraction $(-)$
$\hat{\xi}$	Random number from normal distribution $(-)$
$\langle\gamma\rangle$	Particle wall mean roughness coefficient $(-)$
$\langle\gamma^2\rangle$	Variance of particle wall roughness coefficient $(-)$
μ	Dynamic viscosity of gas $(Pa\cdot s)$
μ_w	Particle wall dynamic friction coefficient $(-)$
ρ_g	Density of gas (kg/m^3)
ρ_p	Density of solid particles (kg/m^3)
ρ_t	Density of target material (kg/m^3)
θ	Angle of cross section in the elbow. 0°: elbow inlet; 90°: outlet $(^\circ)$
ε	Erosion rate kg_p/kg_t
ε_h	Erosion rate of depth eroded per second (m/s)
ε_m	Erosion rate of mass loss of target material per unit area per second $(kg/(m^2\cdot s))$

Acknowledgments

This work was performed using HPC resources of CALMIP under the allocation 2017 2018 and of CINES Occigen under the allocation n°A0022B06012. The financial support of Institut Carnot ISIFoR is grate fully acknowledged. W. YU would like to acknowledge G.V. Messa from DICA of Politecnico di Milano for communicating his results. Great help from H. Neau (IMFT) for technical support on NEPTUNE_CFD is also acknowledged.

Appendix A. Mathematical model for gas-solid turbulent flows

In such an appendix the set of equations of the multi fluid Eulerian model is introduced. Hereafter, the gas phase corresponds to the sub script $k = g$ and the particulate phase to $k = p$.

From the joint fluid particle Probability Density Function (PDF) ap proach [25], the mass balance equation reads

$$\frac{\partial}{\partial t}\alpha_k\rho_k + \frac{\partial}{\partial x_j}\alpha_k\rho_k U_{k,j} \quad 0 \tag{A.1}$$

where α_k is the volume fraction of the phase k, ρ_k the density and $U_{k,\,i}$ the i^{th} component of the k phase mean velocity. We emphasize that $\alpha_p\rho_p$ represents $n_p m_p$ where n_p is the number density of p particle cen ters and m_p the mass of a single p particle. Then $\alpha_p = n_p m_p/\rho_p$ is an ap proximation of the local volume fraction of the dispersed phase. Hence, gas and particle volume fractions α_g and α_p satisfy $\alpha_p + \alpha_g = 1$. The right hand side of Eq. (A.1) is equal to zero because in the present study no mass transfer is taking place.

From the PDF approach, the mean momentum transport equation is written as

$$\alpha_k\rho_k\left[\frac{\partial}{\partial t} + U_{k,j}\frac{\partial}{\partial x_j}\right]U_{k,i} \quad -\alpha_k\frac{\partial P_g}{\partial x_i} + \alpha_k\rho_k g_i + I_{k,i} - \frac{\partial \Sigma_{k,ij}}{\partial x_j} \tag{A.2}$$

where P_g is the mean gas pressure, g_i the gravity and $\Sigma_{k,\,ij}$ the effective stress tensor for which the model closure is described hereafter. The mean gas particle interphase momentum transfer, $I_{k,\,i}$, is written with out the mean gas pressure contribution. In the present study, the large particle to gas density ratio allows to consider that only the drag force acts on the particles. In such a framework, the mean gas particle inter phase momentum transfer term reads:

$$I_{p,i} \quad -\alpha_p\rho_p\frac{V_{r,i}}{\tau_{gp}^F} \quad \text{and} \quad I_{g,i} \quad -I_{p,i} \tag{A.3}$$

where the mean particle relaxation time scale is

$$\frac{1}{\tau_{gp}^F} \quad \frac{3}{4}\frac{\rho_g}{\rho_p}\frac{\langle|v_r|\rangle}{d_p}C_d \ . \tag{A.4}$$

The drag coefficient, C_d, is estimated by using the correlation of [Gobin et al. [31]

$$C_d \quad \begin{cases} \min(C_{d,Erg}, C_{d,WY}) & \text{if } \alpha_p > 0.3 \\ C_{d,WY} & \text{otherwise} \end{cases} \tag{A.5}$$

where $C_{d,\,Erg}$ is the drag coefficient proposed by Ergun [32]:

$$C_{d,Erg} \quad 200\frac{\alpha_p}{Re_p} + \frac{7}{3} \tag{A.6}$$

and $C_{d,\,WY}$ by Wen and Yu [26]:

$$C_{d,WY} \quad \begin{cases} 0.44\alpha_g{}^{1.7} & \text{if } Re_p \geq 1000 \\ \dfrac{24}{Re_p}\left(1 + 0.15\,Re_p^{0.687}\right)\alpha_g{}^{1.7} & \text{otherwise} \end{cases} \tag{A.7}$$

The particle Reynolds number is given by

$$Re_p \quad \alpha_g\frac{\rho_g\langle|v_r|\rangle d_p}{\mu_g}. \tag{A.8}$$

In Eqs. (A.4) & (A.8) the averaged magnitude of the fluid particle rel ative velocity is approximated by $\langle|\mathbf{v}_r|\rangle \approx \sqrt{\langle\mathbf{v}_r^2\rangle} \quad \sqrt{V_{r,i}V_{r,i} + \langle v'_{r,i}v'_{r,i}\rangle}$. The mean gas particle velocity $V_{r,\,i}$, is expressed in terms of the mean gas and solid velocities as $V_{r,\,i} = U_{p,\,i} - U_{f,\,i} - V_{d,\,i}$ where $V_{d,\,i}$ is the

drift velocity:

$$V_{d,i} \quad \frac{1}{3}\tau^t_{gp} q_{gp}\left[\frac{1}{\alpha_p}\frac{\partial \alpha_p}{\partial x_i} - \frac{1}{\alpha_g}\frac{\partial \alpha_g}{\partial x_i}\right] \quad . \tag{A.9}$$

In Eq. (A.9), τ^t_{gp} is the integral time scale of the turbulence seen by the particle and $q_{gp} = \langle u_{p,}{}'_i u_{g,}{}'_i \rangle$ is the fluid particle covariance obtained by solving a specific transport equation. Finally, the fluid particle relative velocity variance writes $\langle v_{r,}{}'_i v_{r,}{}'_i \rangle = 2q_p^2 + 2k - 2q_{gp}$ with the particle kinetic energy, $q_p^2 = \langle u_{p,}{}'_i u_{p,}{}'_i \rangle/2$, and fluid kinetic energy $k = \langle u_{g,}{}'_i u_{g,}{}'_i \rangle/2$. Here, $u'_{p,i}$ is the fluctuating part of the instantaneous solid velocity and $u'_{g,i}$ is the fluctuating part of the instantaneous gas velocity.

The solid stress tensor reads $\Sigma_{p,ij} = \alpha_p \rho_p \langle u'_{p,i} u'_{p,j} \rangle + \Theta_{p,ij}$ where $\Theta_{p,ij}$ is the collisional particle stress tensor. Following Boelle et al. [33], Balzer [34], the particulate stress tensor is expressed as

$$\Sigma_{p,ij} \quad [P_p - \lambda_p D_{p,mm}]\delta_{ij} - 2\mu_p\left[D_{p,ij} - \frac{1}{3}D_{p,mm}\delta_{ij}\right] \tag{A.10}$$

where the strain rate tensor is defined by $D_{p,ij} = 1/2[\partial U_{p,i}/\partial x_j + \partial U_{p,j}/\partial x_i]$. The granular pressure, viscosities and model coefficients are given by

$$P_p \quad \frac{2}{3}\alpha_p \rho_p q_p^2 [1 + 2\alpha_p g_0 (1 + e_c)] \tag{A.11}$$

$$\lambda_p \quad \frac{4}{3}\alpha_p^2 \rho_p d_p g_0 (1 + e_c)\sqrt{\frac{2}{3}\frac{q_p^2}{\pi}} \tag{A.12}$$

$$\mu_p \quad \alpha_p \rho_p \left(\nu_p^k + \nu_p^c\right) \tag{A.13}$$

$$\nu_p^k \quad \left[\frac{1}{3}q_{gp}\tau^t_{gp} + \frac{1}{2}\tau^F_{gp}\frac{2}{3}q_p^2(1 + \alpha_p g_0 \xi)\right] / \left[1 + \frac{\sigma}{2}\frac{\tau^F_{gp}}{\tau_c}\right] \tag{A.14}$$

$$\nu_p^c \quad \frac{4}{5}\alpha_p g_0 (1 + e_c)\left[\nu_p^{kin} + d_p\sqrt{\frac{2}{3}\frac{q_p^2}{\pi}}\right] \tag{A.15}$$

$$\zeta \quad \frac{2}{5}(1 + e_c)(3e_c - 1) \tag{A.16}$$

$$\sigma \quad \frac{1}{5}(1 + e_c)(3 - e_c) \quad . \tag{A.17}$$

The collision time scale, τ_c, is given by

$$\frac{1}{\tau_c} \quad 4\pi g_0 n_q d_p^2 \sqrt{\frac{2}{3\pi}q_p^2} \tag{A.18}$$

where the radial distribution function, g_0, is obtained from Lun and Savage [35],

$$g_0(\alpha_p) \quad \left[1 - \frac{\alpha_p}{\alpha_{max}}\right]^{2.5\alpha_{max}} \tag{A.19}$$

where $\alpha_{max} = 0.64$ is the maximum solid volume fraction for closest packing of a random arrangement of spheres.

The gas turbulence is modeled by a $k - \varepsilon$ model with additional terms to take into account the effect of the particles on turbulence [36].

The solid random kinetic energy transport equation is written:

$$\begin{aligned}\alpha_p \rho_p \left[\frac{\partial q_p^2}{\partial t} + U_{p,j}\frac{\partial q_p^2}{\partial x_j}\right] \quad & \frac{\partial}{\partial x_j}\left[\alpha_p \rho_p \left(K_p^k + K_p^c\right)\frac{\partial q_p^2}{\partial x_j}\right] \\ & - \Sigma_{p,ij}\frac{\partial U_{p,i}}{\partial x_j} \\ & - \frac{\alpha_p \rho_p}{\tau^F_{gp}}\left(2q_p^2 - q_{gp}\right) \\ & - \frac{1}{3}\frac{1 - e_c^2}{\tau_c}\alpha_p \rho_p q_p^2 .\end{aligned} \tag{A.20}$$

In Eq. (A.20), the first term on the right hand side represents the transport of the random particle kinetic energy due to the particle agitation and the collisional effects. The second term on the right hand side of Eq. (A.20) represents the production of particle agitation by the gradients of the mean solid velocity. The third term is the interaction with the gas. Finally the fourth term corresponds to the particle agitation dissipation by inelastic collisions.

In Eq. (A.20) the remaining terms terms are modeled by

$$K_p^k \quad \left[\frac{1}{3}q_{gp}\tau^t_{gp} + \frac{2}{3}q_p^2\frac{5}{9}\tau^F_{gp}(1 + \alpha_p g_0 \zeta_c)\right] / \left[1 + \frac{5}{9}\tau^F_{gp}\frac{\xi_c}{\tau_c}\right] \tag{A.21}$$

$$K_p^c \quad \alpha_p g_0 (1 + e_c)\left[\frac{6}{5}K_p^{kin} + \frac{4}{3}d_p\sqrt{\frac{2}{3}\frac{q_p^2}{\pi}}\right] \tag{A.22}$$

$$\zeta_c \quad \frac{3}{5}(1 + e_c)^2(2e_c - 1) \tag{A.23}$$

$$\xi_c \quad \frac{(1 + e_c)(49 - 33e_c)}{100} . \tag{A.24}$$

Finally a transport equation on the fluid particle covariance, q_{gp} is also solved. Details can be found in Simonin et al. [37]

Appendix B. Validation

The predictive response of empirical erosion models is correlated to the accuracy of impact parameters related to flow dynamics (mean solid volume fraction, particle velocity and turbulence kinetic energy) provided by CFD. To assess the reliability of simulations in pipe bend configuration by NEPTUNE_CFD and to elaborate on the choice of different physical modelling (turbulence model for gas and for solid, the wall boundary conditions etc), two validation cases are presented, one for single phase flow and another for two phase flow.

B.1. Single phase flow in a bend

Turbulent gas flow in a 90° bend (circular cross section) with smooth walls has been investigated experimentally by Sudo et al. [10]. The bend was set horizontally between two straight pipes (upstream (10.4 *m*) and downstream (4.16 *m*)). The 90° bend has a curvature radius $r = 208$ *mm*. The inner diameter of the pipe cross section was $D = 104$ *mm*, the curvature to diameter ratio was $r/D = 2$. The bulk mean velocity of the flow was $V_{gas} = 8.7$ *m/s* with air density $\rho_g = 1.26$ *kg/m*^{3} and dynamic viscosity $\mu = 1.98 \times 10^{-5}$ *Pa · s*, corresponding to a Reynolds number close to 60,000. A structured hexahedral mesh with 93,500 cells has been built. Convergence tests have shown that it was adequate to capture all the flow features. The turbulence model $R_{ij} - \epsilon$ SSG was chosen because of the high degree of anisotropy and significant streamline curvature in flows through the pipe bend.

Fig. 22 shows the static wall pressure coefficient $C_p \quad \frac{(P_g - P_0)}{\frac{1}{2}\rho_g V_{gas}^2}$ along pipe extrados, intrados and at the bottom of the bend. Figs. 23(a) and (b) show the axial velocities U_a in horizontal and vertical planes in the

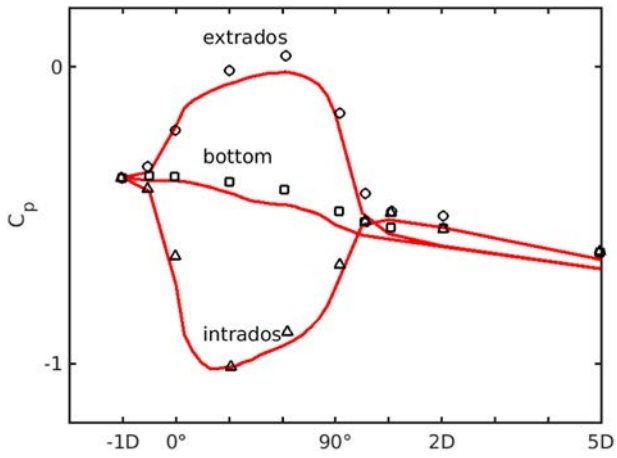

Fig. 22. Static wall pressure coefficient C_p along the pipe bend. Black symbols represent experimental data [38], red lines stand for our numerical results.

bend, respectively. A good agreement between experimental results and our numerical prediction is observed for both wall pressure evolu tion and axial velocities of gas in the bend.

B.2. Two phase flow in a curved channel

After the previous validation for gas flow in a bend configuration, an experimental investigation [39] of dilute turbulent particulate flow in side a 90° curved Perspex channel with square cross section 150 mm $\times$ 150 mm is chosen to validate our modelling of particle characteristics in the bend. The configuration consisted of a 3.5 m horizontal straight duct, a curved 90° bend with $r/D = 1.5$ and a 1.8 m vertical upwards straight duct. Air was flowing at a bulk velocity of $V_{gas} = 10\ m/s$ with the Reynolds number 100,000 based on the bulk velocity and hydraulic diameter of the square cross section. Glass beads with mean diameter of $d_p = 77\ \mu m$ and density $\rho_p = 2500\ kg/m^3$ were used to represent the solid phase. Particles are flowing in a dilute regime of low solid mass loading ($L = 0.00206$). As mentioned by Yang and Kuan [39] and Kuan et al. [40], the feedback effect of particles on gas dynamics and inter particle collisions can be neglected in this study.

The computational domain is composed of 1,135,000 hexahedral cells. The turbulence model $R_{ij} - \epsilon$ SSG for gas is used and the turbu lence model for the solid phase $q_p^2 - q_{fp}$ [25] is chosen assuming that the particle kinetic normal stress is approximated by $\langle u_n' u_n' \rangle \approx 2/3 q_p^2$. Due to high density ratio between glass and air, only drag and inertial forces are taken into account. Considering materials used in experiments of Yang and Kuan [39] (glass for solid particles, Perspex for pipe), a free slip boundary condition is applied for solid phase ($e_w = 1.0$ and $\mu_w = 0.0$) and no wall roughness is considered for this case.

It is important to mention that polydisperse particle size distribution has also been considered in the present simulation: 12 classes of parti cles were used ranging from 5 to 152 μm (details can be found in Table 2 of Kuan et al. [40]).

Gas velocities are well predicted once again at all locations along the bend as shown in Fig. 24(a) and (b). Numerical and experimental pro files of mean axial and radial velocities of solid particles are compared

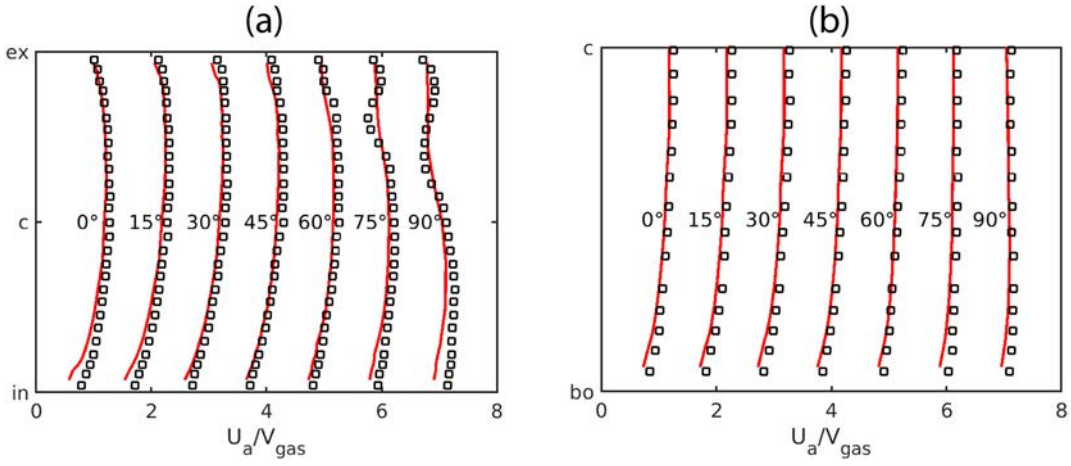

Fig. 23. Velocity profiles in the bend. (a) Axial velocity U_a in horizontal plane. (b) Axial velocity U_a in vertical plane. "ex" represents extrados, "c" for center, "in" for intrados and "bo" for bottom. Black squares represent experimental data [33], red lines are for our numerical results.

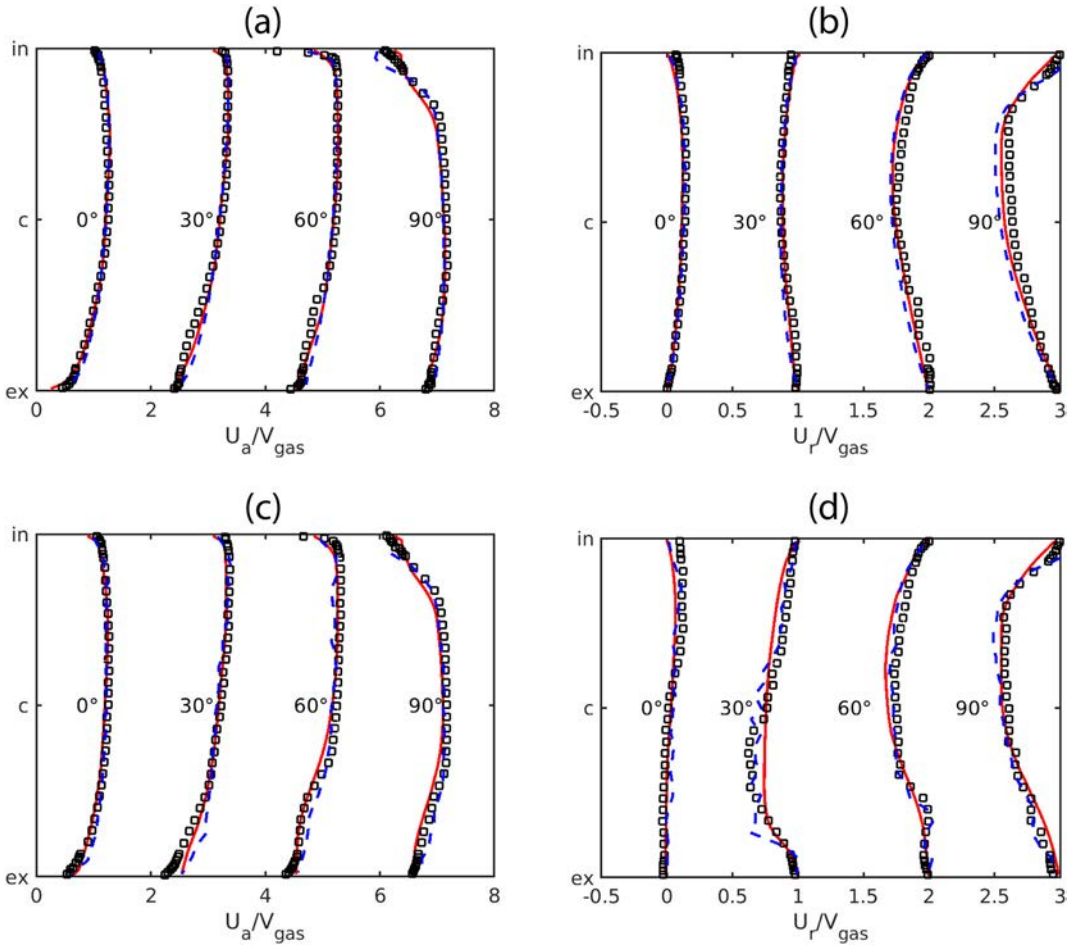

Fig. 24. Velocity profiles along the bend. (a) Axial velocity U_a of gas. (b) Radial velocity U_r of gas. (c) Axial velocity U_a of particles. (d) Radial velocity U_r of particles. "ex" represents extrados, "c" for center and "in" for intrados. Black squares represent experimental data [40], blue dashed lines are numerical results from a previous study [20], red lines represent our numerical results.

in Fig. 24(c) and (d). Overall, the numerical simulation provides a good prediction of the experimental measurements. Compared to numerical results of Kuan et al. [40] based on a Lagrangian particle tracking method, our results are closer to the experimental data in outer wall region (close to extrados), especially for 30° and 60° in Fig. 24(c). This might be related to better prediction of gas velocity in the same region by NEPTUNE_CFD.

Through these two validation cases, we can conclude that the turbulence models for gas and solid selected in NEPTUNE_CFD are suitable to predict gas solid flow within a bend configuration.

References

[1] I. Finnie, Erosion of surfaces by solid particles, Wear 3 (1960) 87–103.
[2] J.G.A. Bitter, A study of erosion phenomena part I, Wear 6 (1963) 5–21.
[3] J.G.A. Bitter, A study of erosion phenomena part II, Wear 6 (1963) 169–190.
[4] R.E. Winter, I.M. Hutchings, Solid particle erosion studies using single angular particles, Wear 29 (1974) 181–194.
[5] M. Parsi, K. Najmi, F. Najafifard, S. Hassani, B.S. McLaury, S.A. Shirazi, A comprehensive review of solid particle erosion modeling for oil and gas wells and pipelines applications, J. Nat. Gas Sci. Eng. 21 (2014) 850–873.
[6] X. Chen, B.S. McLaury, S.A. Shirazi, Application and experimental validation of a computational fluid dynamics (CFD)-based erosion prediction model in elbows and plugged tees, Fluids;Comput. Fluids 33 (2004) 1251–1272.
[7] X. Chen, B.S. McLaury, S.A. Shirazi, Numerical and experimental investigation of the relative erosion severity between plugged tees and elbows in dilute gas/solid two-phase flow, Wear 261 (2006) 715–729.
[8] G.C. Pereira, F.J. de Souza, D.A. de Moro Martins, Numerical prediction of the erosion due to particles in elbows, Powder Technol. 261 (2014) 105–117.
[9] C.A.R. Duarte, F.J. de Souza, V.F. dos Santos, Numerical investigation of mass loading effects on elbow erosion, Powder Technol. 283 (2015) 593–606.
[10] C.B. Solnordal, C.Y. Wong, J. Boulanger, An experimental and numerical analysis of erosion caused by sand pneumatically conveyed through a standard pipe elbow, Wear 336–337 (2015) 43–57.
[11] R.E. Vieira, A. Mansouri, B.S. McLaury, S.A. Shirazi, Experimental and computational study of erosion in elbows due to sand particles in air flow, Powder Technol. 288 (2016) 339–353.
[12] L. Xu, Q. Zhang, J. Zheng, Y. Zhao, Numerical prediction of erosion in elbow based on CFD-DEM simulation, Powder Technol. 302 (2016) 236–246.
[13] A. Uzi, Y. Ben Ami, A. Levy, Erosion prediction of industrial conveying pipelines, Powder Technol. 309 (2017) 49–60.
[14] A. Forder, M. Thew, D. Harrison, A numerical investigation of solid particle erosion experienced within oilfield control valves, Wear 216 (1998) 184–193.
[15] G. Grant, W. Tabakoff, Erosion prediction in turbomachinery resulting from environmental solid particles, J. Aircr. 12 (1975) 471–478.
[16] M. Sommerfeld, N. Huber, Experimental analysis and modelling of particle-wall collisions, Int. J. Multiphase Flow 25 (1999) 1457–1489.
[17] C.A.R. Duarte, F.J. de Souza, R.d.V. Salvo, V.F. dos Santos, The role of inter-particle collisions on elbow erosion, Int. J. Multiphase Flow 89 (2017) 1–22.
[18] A.T.J. Bourgoyne, Experimental study of erosion in diverter systems due to sand production, SPE/IADC Drilling Conference, Society of Petroleum Engineers, 1989.
[19] X. Chen, Application of Computational Fluid Dynamics (CFD) to Single-Phase and Multiphase Flow Simulation and Erosion Prediction, Ph.D. thesis University of Tulsa, 2004.
[20] T. Deng, A.R. Chaudhry, M. Patel, I. Hutchings, M.S.A. Bradley, Effect of particle concentration on erosion rate of mild steel bends in a pneumatic conveyor, Wear 258 (2005) 480–487.
[21] R. Macchini, M.S.A. Bradley, T. Deng, Influence of particle size, density, particle concentration on bend erosive wear in pneumatic vonveyors, Wear 303 (2013) 21–29.
[22] G.V. Messa, G. Ferrarese, S. Malavasi, A mixed Euler–Euler/Euler–Lagrange approach to erosion prediction, Wear 342–343 (2015) 138–153.
[23] G.V. Messa, S. Malavasi, A CFD-based method for slurry erosion prediction, Wear 398–399 (2018) 127–145.
[24] P. Fede, O. Simonin, A. Ingram, 3D numerical simulation of a lab-scale pressurized dense fluidized bed focussing on the effect of the particle-particle restitution coefficient and particle–wall boundary conditions, Chem. Eng. Sci. 142 (2016) 215–235.

[25] O. Simonin, Statistical and Continuum Modelling of Turbulent Reactive Particulate Flows. Lecture Series 6, 2000.
[26] C. Wen, Y. Yu, Mechanics of fluidization, Chem. Eng. Prog. Symp. Ser. 162 (1966) 100–111.
[27] K.R. Ahlert, Effects of Particle Impingement Angle and Surface Wetting on Solid Particle Erosion of AISI 1018 Steel, Ph.D. thesis University of Tulsa, 1994.
[28] G.L. Sheldon, A. Kanhere, An investigation of impingement erosion using single particles, Wear 21 (1972) 195–209.
[29] N. Konan, S. Laìn, O. Simonin, M. Sommerfeld, Comparison between euler-euler and euler-lagrange computations of gas-solid turbulent flow in a horizontal channel with different wall roughness, ASME Joint U.S. - European Fluids Enigneering Summer Meeting, Miami, Floride, USA, 2006.
[30] M. Sommerfeld, J. Kussin, Wall roughness effects on pneumatic conveying of spherical particles in a narrow horizontal channel, Powder Technol. 142 (2004) 180–192.
[31] A. Gobin, H. Neau, O. Simonin, J.R. Llinas, V. Reiling, J.L. Sélo, Fluid dynamic numerical simulation of a gas phase polymerization reactor, Int. J. Numer. Methods Fluids 43 (2003) 1199–1220.
[32] S. Ergun, Fluid flow through packed columns, Chem. Eng. Prog. 48 (1952) 89–94.
[33] A. Boelle, G. Balzer, O. Simonin, Second-order prediction of the particle-phase stress tensor of inelastic spheres in simple shear dense suspensions, ASME FED 228 (1995).
[34] G. Balzer, Gas-solid flow modelling based on the kinetic theory of granular media: validation, applications and limitations, Powder Technol. 113 (2000) 299–309.
[35] C. Lun, S. Savage, The effects of an impact velocity dependent coefficient of restitution on stresses developed by sheared granular materials, Acta Mech. 63 (1986) 539–559.
[36] O. Vermorel, B. Bédat, O. Simonin, T. Poinsot, Numerical study and modelling of turbulence modulation in particle laden slab flow, J. Turbul. 335 (2003) 75–109.
[37] O. Simonin, E. Deutsch, J. Minier, Eulerian prediction of the fluid/particle correlated motion in turbulent two-phase flows, Appl. Sci. Res. 51 (1993) 275–283.
[38] K. Sudo, M. Sumida, H. Hibara, Experimental investigation on turbulent flow in a circular-sectioned 90-degree bend, Exp. Fluids 25 (1998) 42–49.
[39] W. Yang, B. Kuan, Experimental investigation of dilute turbulent particulate flow inside a curved 90° bend, Chem. Eng. Sci. 61 (2006) 3593–3601.
[40] B. Kuan, W. Yang, M.P. Schwarz, Dilute gas–solid two-phase flows in a curved 90° duct bend: CFD simulation with experimental validation, Chem. Eng. Sci. 62 (2007) 2068–2088.